

Computing the CMB power spectrum from the linearly perturbed Einstein-Boltzmann equations*

Brage A. Trefjord

Department of Physics, University of Oslo, Norway

(Dated: May 29, 2024)

In this paper we compute the cosmological microwave background (CMB) power spectrum numerically for a model where we neglect reionization, photon multipoles and neutrinos, and compare it to data provided by the Planck 2018 paper. We start by computing some background cosmological parameters, then we describe the process of recombination and compute when this happens. After this we look at how structures in the universe form by applying linear perturbation theory to a homogeneous and isotropic universe. Lastly, we combine everything we have found to compute the CMB power spectrum, and look at what the different parts of the spectrum describes. The main result of this paper is the predicted CMB power which is somewhat different from observations. This prediction error is, however, consistent with the fact that we did not consider neutrinos when solving for the perturbation parameters, and can be explained by a lack of radiation driving due to the lost pressure contribution that neutrinos would give.

Keywords: Cosmology, Big bang, CMB

I. INTRODUCTION

The most compelling evidence of the big bang theory was the discovery of the cosmic microwave background (CMB) radiation by Penzias and Wilson [1] in 1965. Since then, our understanding of the CMB has improved vastly through more precise experiments, and better and more efficient cosmological models [2]. Understanding the CMB is necessary to further improve our knowledge about what makes up our universe, and how it has evolved from the big bang until today. The most important tool in understanding the CMB is the CMB power spectrum, which describes temperature anisotropies that we measure in the CMB today at different scales. From this power spectrum we are able to infer important cosmological like the density ratios of different constituents such as matter, radiation, dark matter and dark energy; the geometry of the universe, whether it is open, flat or closed; and the inflation epoch in the beginning of our universe.

The main goal of this paper is to compute the CMB power spectrum, and describe what it communicates about the nature of the universe. The road to this goal is split into four milestones.

1. In the first milestone we will look at the background cosmology, computing different time variables and see how the density parameters of different constituents evolve over time, and compare some of the different epochs in the history of our universe, as well as how old the universe is.
2. In the second milestone we will look at recombination, which is when photons decouple from baryons,

and start moving freely. This event is very important, as the photons we observe in the CMB today were freed at this point in time, so what we see is really how the universe looked at recombination.

3. In the third milestone we will look at linear perturbations to the homogeneous and isotropic universe, and look at how structures in the universe formed over time. This is important for us since the CMB is not isotropic, but we measure small variations in photon temperatures in different directions. Understanding perturbations to homogeneity and isotropy is necessary to make sense of these temperature anisotropy.
4. Finally, in the fourth and last milestone, we will compute the CMB power spectrum and compare it to data from the Planck paper [2]. In this milestone we will attempt to explain the physical significance of different parts of the power spectrum, and use the data to evaluate our model. We will also take a look at the matter power spectrum from our model, and compare this to data from the SDSS galaxy surveys [3] and WMAP/ACT [4].

Many of the equations in this paper are copied from Winther's webpage [5], and this is also where most of the physical understanding in this paper stems. We have also had very good use of the paper by Petter Callin [6] in understanding the numerical implementations, and the CMB tutorials on Wayne Hu's webpage [7] in getting a physical intuition for what goes on in the CMB power spectrum.

II. MILESTONE I BACKGROUND COSMOLOGY

In order to compute the CMB power spectrum there are several different values that we will need, and in this

* Github repository: <https://github.com/Bragit123/AST5220>
Email address: b.a.trefjord@fys.uio.no

milestone we have computed some of the most important background parameters needed to deal with the structure and evolution of the universe. This includes the different measures of time, namely cosmic time, conformal time and redshift; the different measures of distance, namely co-moving distance, angular diameter distance and luminosity distance; the Hubble parameter and the conformal Hubble parameter; and the densities of the different constituents that make up the universe, namely photons, neutrinos, baryons, dark matter and dark energy. Lastly, we also tested the theoretical predictions by comparing to observational data from supernovas [8].

A. Theory

1. Time variables

Any value that is monotonically increasing (or decreasing) with time can be used as a measure of the time that has passed since the big bang. Which time variable that is most convenient to work with might vary between different applications. One such time variable is the scalefactor a of the universe. a is defined to be relative size of the universe compared to today. In other words, $a_0 = a(\text{today}) = 1$. We will often have use of the logarithm of the scalefactor, since we want to explore values that vary a lot over small changes in the scalefactor, and we define this as its own time variable, namely

$$x = \log a. \quad (1)$$

In addition, we will need the conformal time η , defined by

$$\frac{d\eta}{dt} = \frac{c}{a}, \quad (2)$$

also called the horizon. η is the distance that light may have travelled since the big bang ($t = 0$). We can rewrite Eq. 2 by substituting $t \rightarrow x$. We then get

$$\frac{d\eta}{dx} = \frac{c}{\mathcal{H}}, \quad (3)$$

where $\mathcal{H} = aH$ is the conformal Hubble parameter, where $H = \frac{\dot{a}}{a}$ is the Hubble parameter. Note here that the dot denotes a derivative with respect to conformal time, i.e., $\dot{} = \frac{d}{d\eta}$.

The cosmic time t is the time experienced by an observer with no velocity, away from any gravitational field, and is given by

$$\frac{dt}{dx} = \frac{1}{H}. \quad (4)$$

The redshift z , defined by

$$1 + z = \frac{1}{a}, \quad (5)$$

is a measure of how much light will have redshifted over time, and is also used as a time variable.

The co-moving distance is

$$\chi(a) = \eta_0 - \eta(a), \quad (6)$$

where η_0 denotes the conformal time today. The co-moving distance is the distance between two points at the present time (i.e., without taking the expansion of the universe into account), namely the distance between the horizon η_0 today, and the horizon $\eta(a)$ at some scalefactor a .

We also have the angular diameter distance

$$d_A = ar, \quad (7)$$

where

$$r = \begin{cases} \chi \cdot \frac{\sin(\sqrt{|\Omega_{k0}|}H_0\chi/c)}{(\sqrt{|\Omega_{k0}|}H_0\chi/c)} & \Omega_{k0} < 0 \\ \chi & \Omega_{k0} = 0 \\ \chi \cdot \frac{\sinh(\sqrt{|\Omega_{k0}|}H_0\chi/c)}{(\sqrt{|\Omega_{k0}|}H_0\chi/c)} & \Omega_{k0} > 0 \end{cases}, \quad (8)$$

which describes the expected distance to an object of known size based on the measured angle it spans. Lastly, we have the luminosity distance

$$d_L = \frac{r}{a} = \frac{d_A}{a^2}, \quad (9)$$

which gives the expected distance to an object of known luminosity, based on the flux measured on earth. Both the angular diameter distance and the luminosity distance are based on euclidean measures of distance.

2. The geometry of the universe

We assume the early universe to be homogeneous and isotropic, and for such a universe we can use the Friedmann-Lemaître-Robertson-Walker (FLRW) metric, which is defined as

$$ds^2 = -c^2 dt^2 + a^2(t)(dx^2 + dy^2 + dz^2), \quad (10)$$

where ds is the line element in spacetime and t and $\vec{x} = (x, y, z)$ are the spacetime components.

The Einstein equation is given by

$$G_{\mu\nu} = 8\pi GT_{\mu\nu}, \quad (11)$$

where $G_{\mu\nu}$ is the Einstein tensor, G is Newton's gravitational constant, and $T_{\mu\nu}$ is the energy-momentum tensor. The Einstein equation relates the geometry of the universe (given by $G_{\mu\nu}$) to the distribution of energy and momentum (given by $T_{\mu\nu}$). The Einstein tensor is given by

$$G_{\mu\nu} = R_{\mu\nu} - \frac{1}{2}Rg_{\mu\nu}, \quad (12)$$

where $R_{\mu\nu}$ is the Ricci tensor, and $R = R^\mu_\mu = g^{\mu\nu}R_{\mu\nu}$ is the Ricci scalar. The Ricci tensor is in turn given by

$$R_{\mu\nu} = \Gamma_{\mu\nu,\alpha}^\alpha - \Gamma_{\mu\alpha,\nu}^\alpha + \Gamma_{\mu\nu}^\alpha \Gamma_{\alpha\beta}^\beta - \Gamma_{\mu\alpha}^\beta \Gamma_{\beta\nu}^\alpha,$$

where

$$\Gamma_{\alpha\beta}^\mu = \frac{g^{\mu\delta}}{2}(g_{\delta\beta,\alpha} + g_{\alpha\delta,\beta} - g_{\alpha\beta,\delta}) \quad (13)$$

are the Christoffel symbols, and a comma in the indices denotes a derivative with respect to some spacetime coordinate, i.e., $\Gamma_{\mu\nu,\beta}^\alpha = \frac{\partial}{\partial x^\beta} \Gamma_{\mu\nu}^\alpha$. From expanding $G_{\mu\nu}$ it becomes clear that it is just made up of the metric tensor (although quite a few of it), which shows how Eq. 11 is related to the geometry of the universe.

3. The constituents of the universe

We assume that every constituent in the universe behave like perfect fluids. The energy-momentum tensor for a perfect fluid is

$$T_{\mu\nu} = (\rho + p)u_\mu u_\nu + pg_{\mu\nu}, \quad (14)$$

where ρ is the energy density of the fluid, p is the pressure, u_μ is the 4-velocity of the fluid, and $g_{\mu\nu}$ is the metric tensor, which in the FLRW metric is given by $g_{00} = -1$, $g_{ij} = a^2(t)\delta_{ij}$ and any other component is zero.

If we insert the FLRW metric tensor $g_{\mu\nu}$ and the energy-momentum tensor $T_{\mu\nu}$ into Eq. 11, we get the Friedmann equation for the Hubble parameter $H = \frac{\dot{a}}{a}$, given by Eq. 15a. From this equation, we can compute the conformal Hubble parameter $\mathcal{H} = aH$, and its derivatives with respect to x . The Hubble parameter H , the conformal Hubble parameter \mathcal{H} and its derivatives $\frac{d\mathcal{H}}{dx}$ and $\frac{d^2\mathcal{H}}{dx^2}$ are given by

$$H = H_0 \sqrt{(\Omega_{b0} + \Omega_{\text{CDM}0})e^{-3x} + (\Omega_{\gamma0} + \Omega_{\nu0})e^{-4x} + \Omega_{k0}e^{-2x} + \Omega_{\Lambda0}}, \quad (15a)$$

$$\mathcal{H} = e^x H, \quad (15b)$$

$$\frac{d\mathcal{H}}{dx} = \frac{H_0^2}{\mathcal{H}} \left[\Omega_{\Lambda0}e^{2x} - (\Omega_{\gamma0} + \Omega_{\nu0})e^{-2x} - \frac{1}{2}(\Omega_{b0} + \Omega_{\text{CDM}0})e^{-x} \right], \quad (15c)$$

$$\frac{d^2\mathcal{H}}{dx^2} = \frac{H_0^2}{\mathcal{H}} \left[2\Omega_{\Lambda0}e^{2x} + 2(\Omega_{\gamma0} + \Omega_{\nu0})e^{-2x} + \frac{1}{2}(\Omega_{b0} + \Omega_{\text{CDM}0})e^{-x} \right] - \frac{1}{\mathcal{H}} \left(\frac{d\mathcal{H}}{dx} \right)^2, \quad (15d)$$

where $H = \frac{\dot{a}}{a}$ is the Hubble parameter (the dot refers to derivative with respect to conformal time $\frac{d}{d\eta}$), $\Omega_i = \frac{\rho_i}{\rho_c}$ ($\rho_c = \frac{3H_0^2}{8\pi G}$ is the critical density) are the density parameters for the different constituents and a subscript 0 refers to the value today. The possible values of i are b (baryons), CDM (cold dark matter), γ (photons), ν (neutrinos), k (curvature) and Λ (dark energy). The density parameters $\Omega_{\gamma0}$ and $\Omega_{\nu0}$ can be computed from the observed CMB temperature. We have

$$\Omega_{\gamma0} = 2 \cdot \frac{\pi^2}{30} \frac{(k_b T_{\text{CMB}0})^4}{\hbar^3 c^5} \cdot \frac{8\pi G}{3H_0^2}, \quad (16a)$$

$$\Omega_{\nu0} = N_{\text{eff}} \cdot \frac{7}{8} \cdot \left(\frac{4}{11} \right)^{4/3} \Omega_{\gamma0}, \quad (16b)$$

where k_b is the Boltzmann's constant, $T_{\text{CMB}0}$ is the CMB temperature today and N_{eff} is the effective number of massless neutrinos.

From Einstein's equations we can also derive the following equation,

$$\frac{d\rho}{dt} + 3H(\rho + p) = 0. \quad (17)$$

Eqs. 15a and 17 are referred to as the Friedmann equations.

If we define the equation of state $\omega = \frac{p}{\rho}$, we can use Eq. 17 to find how the density parameters evolve as functions of the scalefactor a . We find the following

$$\Omega_k(a) = \frac{\Omega_{k0}}{a^2 H(a)^2 / H_0^2} \quad (18a)$$

$$\Omega_{\text{CDM}}(a) = \frac{\Omega_{\text{CDM}0}}{a^3 H(a)^2 / H_0^2} \quad (18b)$$

$$\Omega_b(a) = \frac{\Omega_{b0}}{a^3 H(a)^2 / H_0^2} \quad (18c)$$

$$\Omega_\gamma(a) = \frac{\Omega_{\gamma0}}{a^4 H(a)^2 / H_0^2} \quad (18d)$$

$$\Omega_\nu(a) = \frac{\Omega_{\nu0}}{a^4 H(a)^2 / H_0^2} \quad (18e)$$

$$\Omega_\Lambda(a) = \frac{\Omega_{\Lambda0}}{H(a)^2 / H_0^2}. \quad (18f)$$

4. Analytic expressions in certain regimes

It is important to be able to test the results from our numerical computations, and one way of doing this is to compute analytical expressions in certain regimes that we can compare the numerical results with. Here, we have found some analytical expressions for the radiation dominated era and the dark energy dominated era. We have also included an expression that relates the acceleration of the universe to the conformal Hubble parameter.

a. Radiation dominated era. In very early times, the universe is thought to be radiation dominated, i.e., it consisted mainly of photons and neutrinos. In this regime, one finds that the conformal Hubble parameter \mathcal{H} , and its first and second order derivative with respect to x , are given by

$$\mathcal{H}_R = H_0 e^{-x} \quad (19a)$$

$$\frac{1}{\mathcal{H}_R} \frac{d\mathcal{H}_R}{dx} = -1 \quad (19b)$$

$$\frac{1}{\mathcal{H}_R} \frac{d^2\mathcal{H}_R}{dx^2} = 1. \quad (19c)$$

The conformal time η in the radiation dominated regime is found to be

$$\eta_R(x) = \frac{c}{H_0} e^x, \quad (20)$$

and putting Eq. 19a and 20 together we find that

$$\frac{\eta_R \mathcal{H}_R}{c} = 1, \quad (21)$$

b. Matter dominated era. As with the radiation dominated era, we can find some analytical expressions for a matter dominated universe, i.e., when the universe mainly consisted of baryons and dark matter. In this regime, the conformal Hubble parameter and its derivatives are

$$\mathcal{H}_M = H_0 e^{-\frac{1}{2}x} \quad (22a)$$

$$\frac{1}{\mathcal{H}_M} \frac{d\mathcal{H}_M}{dx} = -\frac{1}{2} \quad (22b)$$

$$\frac{1}{\mathcal{H}_M} \frac{d^2\mathcal{H}_M}{dx^2} = \frac{1}{4}. \quad (22c)$$

c. Dark energy dominated era. We can also find some analytical expressions for a dark energy dominated universe. When the universe mainly consists of dark energy, the conformal Hubble parameter \mathcal{H} and its derivatives with respect to x are

$$\mathcal{H}_{DE} = H_0 e^x \quad (23a)$$

$$\frac{1}{\mathcal{H}_{DE}} \frac{d\mathcal{H}_{DE}}{dx} = 1 \quad (23b)$$

$$\frac{1}{\mathcal{H}_{DE}} \frac{d^2\mathcal{H}_{DE}}{dx^2} = 1. \quad (23c)$$

d. Acceleration of the universe. At a certain point, the expansion of the universe begins to accelerate. a is the scalefactor of the universe, and \ddot{a} is the acceleration of the scalefactor with respect to conformal time η , so the expansion of the universe accelerates if $\ddot{a} > 0$. We can relate this acceleration to the conformal Hubble parameter \mathcal{H} by

$$\ddot{a} = \frac{d\dot{a}}{d\eta} = \frac{d\dot{a}}{dx} \frac{dx}{d\eta} = \frac{d\mathcal{H}}{dx} \frac{1}{\frac{d\eta}{dx}} = \frac{\mathcal{H}}{c} \frac{d\mathcal{H}}{dx}.$$

\mathcal{H} is always positive, thus $\ddot{a} > 0$ if and only if $\frac{d\mathcal{H}}{dx} > 0$, and so the universe is accelerating when $\frac{d\mathcal{H}}{dx} > 0$.

B. Implementation details

In the numerical calculations we have used the parameters that were found as best fits in the Planck paper [2]. These values are

$$\begin{aligned} h &= 0.67, \\ T_{\text{CMB}0} &= 2.7255 \text{ K}, \\ N_{\text{eff}} &= 3.046, \\ \Omega_{b0} &= 0.05, \\ \Omega_{\text{CDM}0} &= 0.267, \\ \Omega_{k0} &= 0, \\ \Omega_{\Lambda 0} &= 1 - (\Omega_{k0} + \Omega_{b0} + \Omega_{\text{CDM}0} + \Omega_{\gamma 0} + \Omega_{\nu 0}), \end{aligned}$$

where h is defined such that $H_0 = 100 h \text{ km}/(\text{s Mpc})$. From these values we also computed Ω_γ and Ω_ν using Eq. 16.

Using these values we computed the Hubble H , the conformal Hubble parameter \mathcal{H} , and the first and second derivatives of \mathcal{H} for different values of x using Eqs. 15. We found the co-moving distance χ using Eq. 6, the angular diameter distance d_A using Eq. 7 and the luminosity distance d_L using Eq. 9

In order to compute the conformal time η and the cosmic time t we used a Runge-Kutta 4 ODE solver to solve Eq. 3 and 4, and created cubic splines for both η and t .

Lastly, we looked at observational data from supernovas, taken from [8]. This dataset consisted of the luminosity distance of the supernovas for different redshifts (together with their errors). We used a Markov chain Monte Carlo (MCMC), namely the Metropolis algorithm [9], to sample from this dataset. Each sample of the MCMC algorithm gave us a χ^2 -, h -, Ω_M - and Ω_K -value, where χ^2 is the chi-squared function and $\Omega_M = \Omega_b + \Omega_{\text{CDM}}$ is the matter density parameter. From Ω_M and Ω_K we found $\Omega_\Lambda = 1 - \Omega_M - \Omega_K$ (here we assume that there is no radiation at the relevant redshifts). We found which samples were within the 1σ and 2σ confidence regions of the samples (σ referring to the standard deviation), by comparing the χ^2 values to the 1σ and 2σ constraints given by [10]. We do the fitting with three free

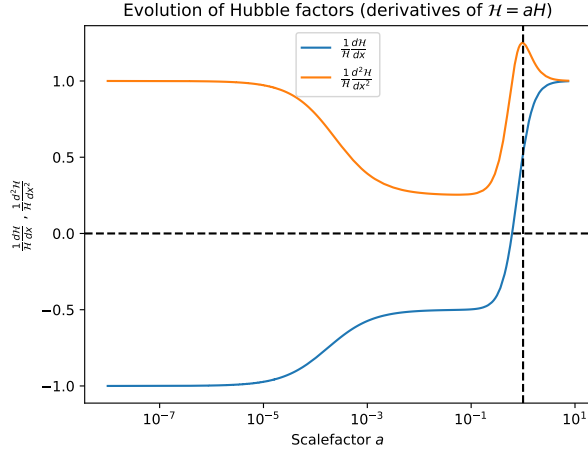


FIG. 1. First and second derivatives of the conformal Hubble factor \mathcal{H} as functions of the scalefactor a . The vertical line at $a = 1$ shows the present day. The horizontal line at $y = 0$ shows where the derivative $\frac{1}{\mathcal{H}} \frac{d\mathcal{H}}{dx} = 0$.

parameters, thus the 1σ confidence region is given by the samples where $\chi^2 - \chi_{\min}^2 < 3.53$, and the 2σ confidence region is given by the samples where $\chi^2 - \chi_{\min}^2 < 8.02$. Here χ_{\min}^2 denotes the smallest χ^2 -value across the samples.

C. Results

In Fig. 1 we have plotted the first and second derivatives of the conformal Hubble factor \mathcal{H} . We see that $\frac{1}{\mathcal{H}} \frac{d\mathcal{H}}{dx} \rightarrow -1$, and $\frac{1}{\mathcal{H}} \frac{d^2\mathcal{H}}{dx^2} \rightarrow 1$, as $a \rightarrow 0$, which corresponds with Eqs. 19 for a radiation dominated universe. This is exactly what we expect for $a \rightarrow 0$, since the early universe was radiation dominated. We also see that both the first and second derivatives converge to 1 as a becomes large. This corresponds well with Eqs. 23 for a dark energy dominated universe, which is what we expect the universe to be as time evolves. The point where $\frac{1}{\mathcal{H}} \frac{d\mathcal{H}}{dx} = 0$ shows the time where the expansion of the universe starts to accelerate.

In Fig. 2 we have plotted the product $\frac{\eta\mathcal{H}}{c}$ as a function of the scalefactor a . We see that $\frac{\eta\mathcal{H}}{c} \rightarrow 1$ as $a \rightarrow 0$, which corresponds well with Eq. 21 for the radiation dominated early universe.

In Fig. 3 you can see how the conformal Hubble factor \mathcal{H} evolves with the scalefactor a . The curve decreases exponentially to start with (straight line in the log-log plot), which corresponds well with Eq. 19a for a radiation dominated universe. After a while, the slope in Fig. 3 changes, and at $a = 0.62$ (shown with a vertical dotted line), \mathcal{H} begins to increase exponentially. The point where \mathcal{H} starts to increase exponentially corresponds to the universe beginning to accelerate.

In Fig. 4 we have plotted the cosmic time t as a function

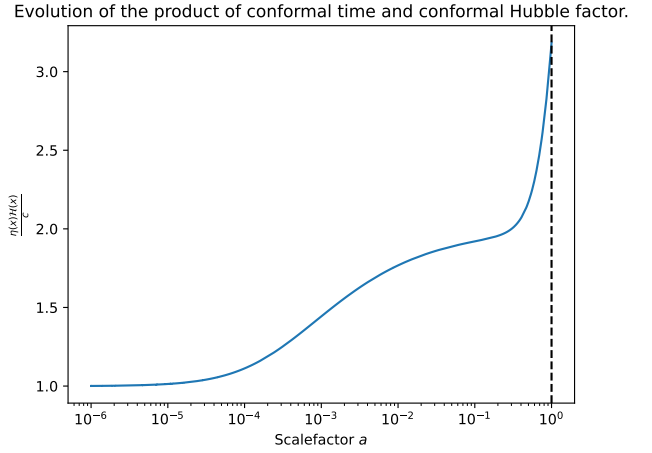


FIG. 2. $\frac{\eta\mathcal{H}}{c}$ as a function of the scalefactor a . The vertical line at $a = 1$ shows the present day.

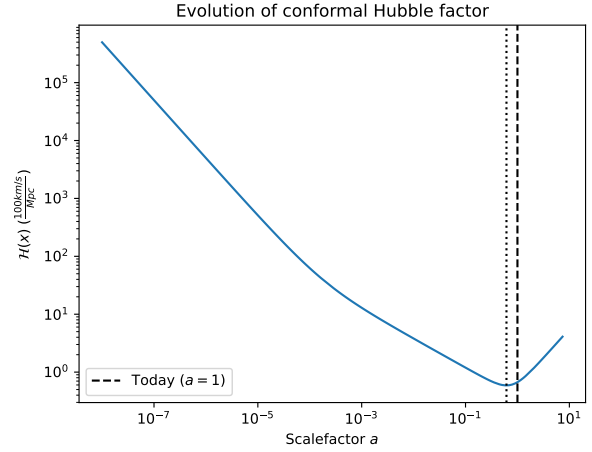


FIG. 3. The conformal Hubble factor \mathcal{H} as a function of the scalefactor a . The vertical dotted line at $a = 0.62$ corresponds to the point where the universe begins to accelerate, and the vertical dashed line at $a = 1$ shows the present day.

of the scalefactor a . From this plot we can clearly see that the universe expands with time, which is a good confirmation that our use of the scalefactor as a time variable is sensible. At $a = 0.62$ (represented by the vertical dotted line) the curve starts to bend downwards. This corresponds to the point where the expansion of the universe begins to accelerate.

The evolution of the conformal time η as a function of the scalefactor a is shown in Fig. 5. The conformal time increases with the scalefactor, which fits well with the conformal time corresponding to the radius of the observable universe. We can also see that the conformal time increases exponentially in the beginning (linearly in the log-log plot), in accordance with Eq. 20 for a radiation dominated universe.

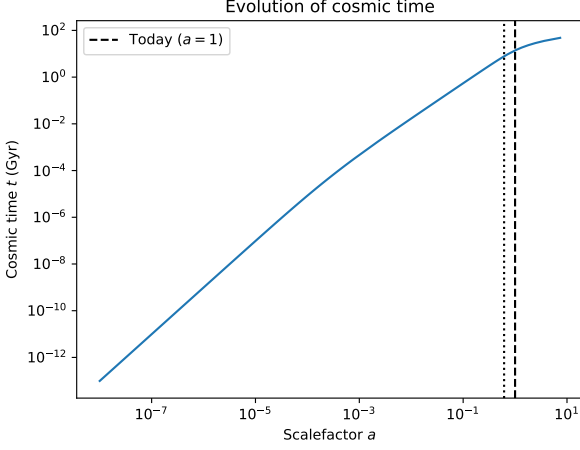


FIG. 4. Cosmic time t as a function of the scalefactor a . The vertical dotted line at $a = 0.62$ corresponds to the point where the universe begins to accelerate, and the vertical dashed line at $a = 1$ shows the present day.

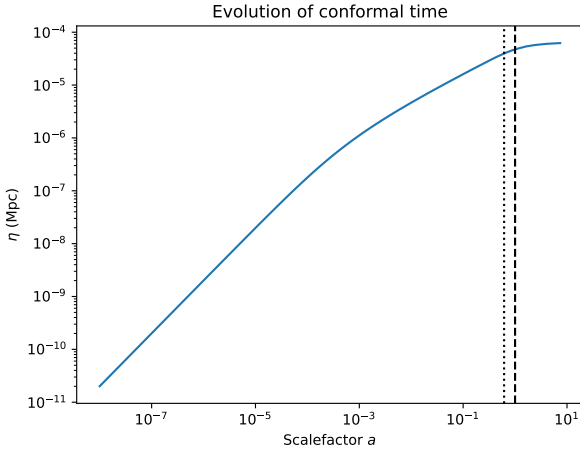


FIG. 5. Conformal time η as a function of the scalefactor a . The vertical line at $a = 1$ shows the present day.

In Fig. 6 we have the density parameters for the different constituents of the universe as functions of the scalefactor a . From the plot we can see that the beginning of the universe was radiation dominated, that is, most of the universe consisted of photons and neutrinos. As the universe expanded, the radiation density decreased, and the matter density increased. In other words, the amount of baryons and cold dark matter increased. After a while, the amount of matter also started to decrease, and the dark energy density started increasing. Today (shown as a vertical dashed line in the figure), dark energy makes up most of the universe, while the rest of the universe consists mainly of baryons and cold dark matter.

The luminosity distance d_L from the supernova dataset [8] is shown in Fig. 7 as a function of redshift z , together

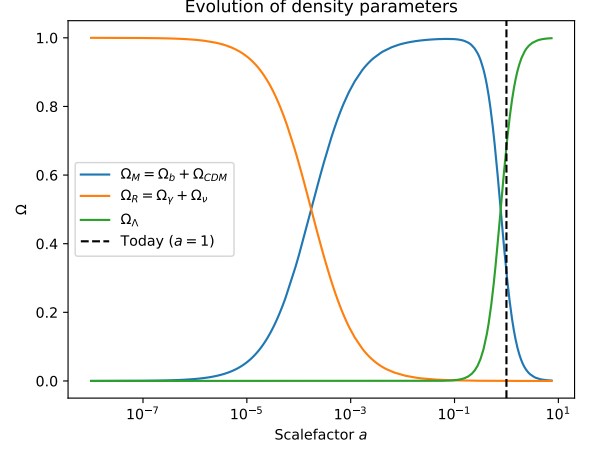


FIG. 6. Density parameters for matter Ω_M , radiation Ω_R and dark energy Ω_Λ as functions of the scalefactor a . The vertical line at $a = 1$ shows the present day.

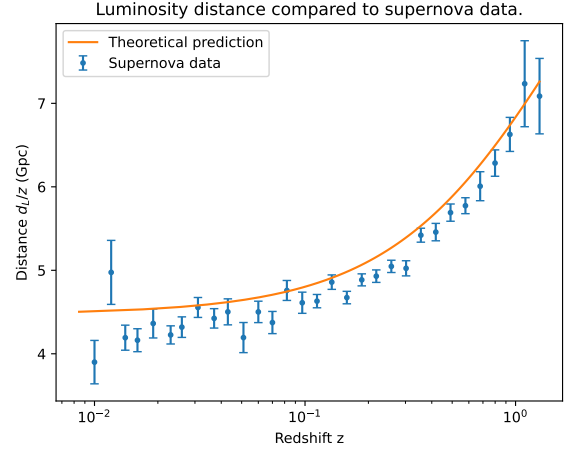


FIG. 7. Comparison of the scaled luminosity distance $\frac{d_L}{z}$ as a function of redshift z , between the supernova data and our theoretical prediction. The supernova data is retrieved from [8].

with the theoretical prediction from our code. The theoretical prediction is not a perfect fit to the dataset. It follows a similar trend, as the curve bends upward in the same manner as the datapoints, but it lies outside the errorbars of quite a few of the datapoints.

In Fig. 8 we have a scatter plot showing the value of Ω_M and Ω_Λ for each sample in the MCMC simulation. The plot shows constraints on the fraction of matter and dark energy in the universe. In other words, according to the simulation, the fraction of matter and dark energy in the universe is very unlikely to be outside the points shown in the figure. More precisely, the 1σ constraint contains 68.3% of the samples, and the 2σ constraint contains 95.45% of the samples [10]. The scatter plot

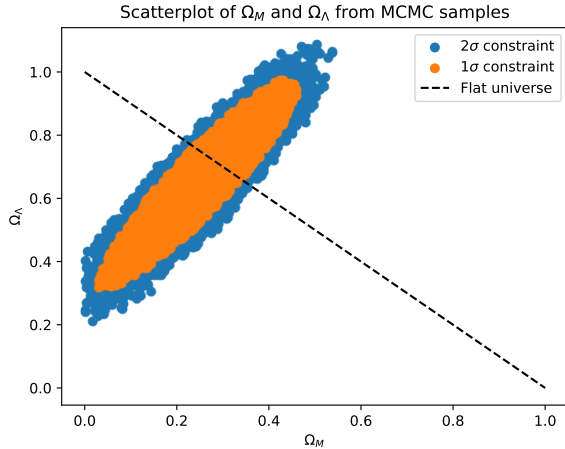


FIG. 8. Distribution of density parameters for matter Ω_M and dark energy Ω_Λ from the Markov chain Monte Carlo (MCMC) method. Each point plotted in the figure represents Ω_M and Ω_Λ for one MCMC sample. The 1σ and 2σ constraints refers to what samples we have included in the plot, namely the values corresponding to χ^2 being within one and two standard deviations respectively. The dashed line shows every value where $\Omega_M + \Omega_\Lambda = 1$, i.e., where the universe consists of only matter and dark energy, thus where the universe is flat.

does not appear to restrict the possible matter-dark energy fraction very much. If we had included results from other observations as well, the samples from the different observations would intersect each other, and in that way restrict the possible fractions further, as shown in [8]. Although Fig. 8 does not restrict the matter-dark energy fraction too much, it does seem to imply very strongly that the dark energy density is non-zero. In other words, the observational data presented in [8] is a strong indication of the existence of dark energy, and thereby the acceleration of the universe.

In Fig. 9 we have plotted a histogram, showing the probability distribution for the Hubble parameter H_0 from the different samples in the MCMC simulation. The normal distribution plotted together with the histogram fits well with the samples, showing that the samples are normally distributed. The best fit value from the MCMC simulation is 0.70. This is way higher than the Planck best fit of 0.67 [2], which is not even shown in Fig. 9. It would be very interesting to further examine why our results deviate so greatly from [2].

In Table I we have included some specific values of time variables at four different times in the history of the universe. We see that the matter-radiation equality happened very early in the universe, after only $2.0 \cdot 10^{-5}$ Gyr after the big bang, or 20 000 years. At this point the universe was only $1.7 \cdot 10^{-4}$ the size of today, with the observable universe reaching $\eta = 86.8$ Mpc in radius. The redshift is very large at $z = 5.75 \cdot 10^3$, which corresponds to light at this time being highly redshifted today after traveling for so long in an expanding universe. 7.76 Gyr

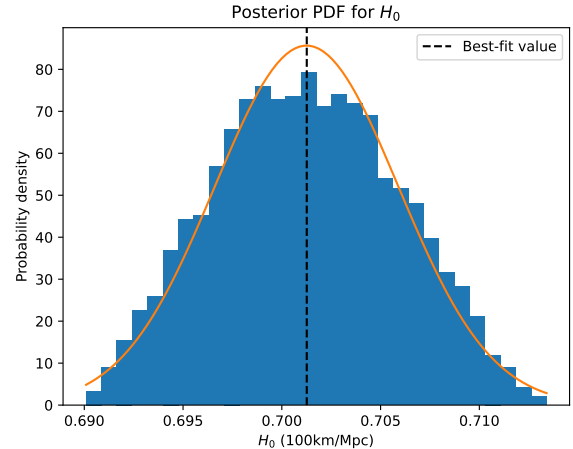


FIG. 9. Histogram showing the frequency of different values of the Hubble parameter H_0 from the Markov chain Monte Carlo (MCMC) samples. The vertical line shows the best fit value of H_0 , i.e., the value corresponding to the sample with the lowest χ^2 value. The orange curve shows a normal distribution corresponding to the mean value and standard deviations of H_0 from the across the MCMC samples.

after the big bang, the universe began to accelerate. At this point the universe was 0.61 the size it is today, and the observable universe had a radius of $\eta = 11.9$ Gpc. The redshift at this point has also decreased largely since the matter-radiation equality epoch, at $z = 0.63$. The next epoch was when the amount of matter and the amount of dark energy were equal. This happened 10.38 Gyr after the big bang, and at this point the size of the universe was 0.77 of what it is today. The observable universe was $\eta = 13.0$ Gpc in radius, and the redshift had dropped to $z = 0.29$.

The last row in Table I shows the time variables' values today, at scalefactor $a = 1$. The redshift is $z = 0.0$, since light emitted today will not be redshifted due to the expansion of the universe when it hits us. The time $t = 13.86$ Gyr is our estimate of the age of the universe based on the numerical computations. This estimate is fairly close to the value of 13.80 Gyr obtained by [2]. This corresponds to a relative error of only 0.4%. We found the radius of the observable universe today to be $\eta = 14.3$ Gpc, which (up to decimal precision) coincides perfectly with the value of 14 Gpc given by [11].

III. MILESTONE II RECOMBINATION HISTORY

The early universe was very hot and dense, consisting of high-energy photons and free electrons. It was essentially opaque, since any photons propagating through space could not move very far before scattering off the free electrons and change direction. As the universe got colder, electrons were able to bind to protons, forming

TABLE I. Values of different time variables at certain points in time. The first row shows when we have matter-radiation equality. The second row shows when the universe begins to accelerate (i.e, when $\frac{dH}{dx} = \dot{a}$ becomes positive). The third row shows when we have matter-dark energy equality. The last row shows the value of the time variables today. The rows are sorted by increasing time. The first column shows the scalefactor a . The second column shows the redshift z . The third column shows the cosmic time t , and the last column shows the conformal time η .

	a	z	t (Gyr)	η (Mpc)
$\Omega_M = \Omega_R$	$1.7 \cdot 10^{-4}$	$5.75 \cdot 10^3$	$2.0 \cdot 10^{-5}$	86.8
Universe accelerates	0.61	0.63	7.76	$1.19 \cdot 10^4$
$\Omega_M = \Omega_\Lambda$	0.77	0.29	10.38	$1.30 \cdot 10^4$
Today	1.0	0.0	13.86	$1.43 \cdot 10^4$

hydrogen atoms, without high-energy photons ripping them apart. This period in the history of the universe is known as recombination, and leads to photons being able to travel further distances without scattering off free electrons, and the universe became transparent. The recombination period is very important for us in understanding the CMB power spectrum, since the CMB is radiation that has traveled to us from the opaque universe just before recombination. In this milestone we look at the time when recombination happens. We compute the free electron fraction of the universe at different times, as well as the optical depth and visibility functions, and use these values to compute what times decoupling and recombination happens. We also compute the sound-horizon at decoupling, since this value will be relevant for the next parts of the project.

A. Theory

1. The Boltzmann equation

When finding the time of recombination, we want to know how many particles of different types that are

present at any time. For this, we have the distribution function $f(t, \vec{x}, \vec{p})$, which gives the number of particles of a particular type. The evolution of f is given by the Boltzmann equation,

$$\frac{df}{dt} = C[f], \quad (24)$$

where $C[f]$ is the collision term, telling us how the particle interacts with other particles. Expanding the left hand side of the equation, we get

$$\frac{\partial f}{\partial t} + \frac{\partial f}{\partial x^i} \frac{dx^i}{dt} + \frac{\partial f}{\partial E} \frac{dE}{dt} + \frac{\partial f}{\partial \hat{p}^i} \frac{d\hat{p}^i}{dt} = C[f]. \quad (25)$$

The collision term we will work with is that of the process $1 + 2 \leftrightarrow 3 + 4$, for which the collision term is

$$\begin{aligned} C(f_1) = & \int \frac{d^3 p_2}{(2\pi)^3 2E_2} \int \frac{d^3 p_3}{(2\pi)^3 2E_3} \int \frac{d^3 p_4}{(2\pi)^3 2E_4} \times \\ & \times |\mathcal{M}|^2 (2\pi) \delta(E_1 + E_2 - E_3 - E_4) (2\pi)^3 \delta^{(3)}(\vec{p}_1 + \vec{p}_2 - \vec{p}_3 - \vec{p}_4) \times \\ & \times [f_3 f_4 (1 \pm f_1)(1 \pm f_2) - f_1 f_2 (1 \pm f_3)(1 \pm f_4)], \end{aligned} \quad (26)$$

where \mathcal{M} is the matrix element of the interaction (related to the probability of the interaction happening), $\delta(x)$ and $\delta^{(3)}(x)$ are the one- and three-dimensional Dirac delta functions, and the indices 1, 2, 3 and 4 correspond to the different particles of the interaction.

2. The Saha equation

Electrons and protons come together to form hydrogen atoms, and high-energy photons cause hydrogen atoms to split back into free electrons and protons. This interaction can be represented as



The universe is electrically neutral, which gives $n_e = n_p$, where n_i is the number density of constituent i . In this

report, we assume that the only atoms being formed in the universe are hydrogen atoms, i.e. we neglect helium and heavier atoms. This gives us the the number density for baryons,

$$n_b \approx n_H = \frac{\rho_b}{m_H} = \frac{\Omega_{b0}\rho_{c0}}{m_H a^3} \quad (28)$$

where m_H is the hydrogen mass, and $\rho_{c0} = \frac{3H_0^2}{8\pi G}$ is the critical density today. We want to find the number density of electrons, and do this by defining the free electron density $X_e = \frac{n_e}{n_b}$. The free electron density will then give us the fraction of the baryons today that are electrons, meaning X_e will be between 0 and 1. In other words, if $X_e = 1$, there are no hydrogens in the universe, and all electrons are free. If $X_e = 0$ there are no free electrons, since they are all bound to atoms.

Using Eq. 25 and Eq. 26, and assuming that the interactions are close to equilibrium, we arrive at the Saha equation

$$\frac{X_e^2}{(1 - X_e)} = \frac{1}{n_b} \left(\frac{k_b T m_e}{2\pi \hbar^2} \right)^{3/2} e^{-\frac{\epsilon_0}{k_b T}}, \quad (29)$$

where m_e is the electron mass, k_b is the Boltzmann's constant, \hbar is Planck's constant, and ϵ_0 is the electric permittivity in vacuum.

3. The Peebles equation

Eq. 29 is an approximation, and it is only valid when we are close to equilibrium. When we move away from equilibrium, we will switch to the Peebles equation given by

$$\frac{dX_e}{dx} = \frac{C_r(T_b)}{H} \left[\beta(T_b)(1 - X_e) - n_H \alpha^{(2)}(T_b) X_e^2 \right]. \quad (30)$$

The expressions for the parameters in the Peebles equation are given by

$$C_r(T_b) = \frac{\Lambda_{2s \rightarrow 1s} + \Lambda_\alpha}{\Lambda_{2s \rightarrow 1s} + \Lambda_\alpha + \beta^{(2)}(T_b)}, \quad (31a)$$

$$\Lambda_{2s \rightarrow 1s} = 8.227 \text{s}^{-1}, \quad (31b)$$

$$\Lambda_\alpha = H \frac{(3\epsilon_0)^3}{(8\pi)^2 c^3 \hbar^3 n_{1s}}, \quad (31c)$$

$$n_{1s} = (1 - X_e) n_H, \quad (31d)$$

$$n_H = n_b = \frac{3H_0^2 \Omega_{b0}}{8\pi G m_H a^3}, \quad (31e)$$

$$\beta^{(2)}(T_b) = \beta(T_b) e^{\frac{3\epsilon_0}{4k_b T_b}}, \quad (31f)$$

$$\beta(T_b) = \alpha^{(2)}(T_b) \left(\frac{m_e k_b T_b}{2\pi \hbar^2} \right)^{3/2} e^{-\frac{\epsilon_0}{k_b T_b}}, \quad (31g)$$

$$\alpha^{(2)}(T_b) = \frac{8}{\sqrt{3\pi}} c \sigma_T \sqrt{\frac{\epsilon_0}{k_b T_b}} \phi_2(T_b), \quad (31h)$$

$$\phi_2(T_b) = 0.448 \ln \left(\frac{\epsilon_0}{k_b T_b} \right). \quad (31i)$$

4. The optical depth

When light moves through a medium, some of the photons will be absorbed, reducing the overall intensity. If the light was emitted from a source with intensity I_0 , then an observer at a time x will observe an intensity of

$$I(x) = I_0 e^{-\tau(x)}, \quad (32)$$

where $\tau(x)$ is called the optical depth. The larger the optical depth is, the less one would see, so $\tau \gg 1$ means we would see nothing, and $\tau \ll 1$ means it would be as if the medium wasn't there. In our case, the medium light travels through is a universe consisting of free electrons, thus the observed intensity is low when the density of free electrons are high, and vice versa. We can find the optical depth from the differential equation

$$\frac{d\tau}{dx} = -\frac{cn_e \sigma_T}{H}, \quad (33)$$

where $\sigma_T = \frac{8\pi}{3} \frac{\alpha^2 \hbar^2}{m_e^2 c^2}$ is the Thomson scattering cross section given by particle physics, and α is the fine-structure constant.

5. The visibility function

From the optical depth we can define the visibility function

$$\tilde{g}(x) = \frac{d}{dx} e^{-\tau} = -\frac{d\tau}{dx} e^{-\tau}. \quad (34)$$

The visibility function is a probability distribution, telling us what the probability that some photon was last scattered at time x . Since \tilde{g} is a probability distribution, it must be normalized, i.e., it must satisfy

$$\int_{-\infty}^0 \tilde{g}(x) dx = 1. \quad (35)$$

6. The sound-horizon

We also want to compute the sound-horizon at decoupling r_s , which is the distance a sound-wave can travel in the photon-baryon plasma from the big bang until photons decouple. The sound-horizon $s(x)$ at a time x is given by

$$\frac{ds(x)}{dx} = \frac{c_s}{\mathcal{H}}, \quad (36)$$

where $c_s = c \sqrt{\frac{R}{3(1+R)}}$, and $R = \frac{4\Omega_{\gamma 0}}{3\Omega_{b0} a}$. Thus the sound-horizon at decoupling is given by $r_s = s(x_{\text{decoupling}})$.

B. Implementation details

We first computed the free electron fraction X_e using the Saha equation, Eq. 29, and the Peebles equation Eq. 30. First, we rewrote Eq. 29 in a way that is more familiar for quadratic equations,

$$X_e^2 + c(x)X_e - c(x) = 0, \quad (37)$$

with

$$c(x) = \frac{1}{n_b} \left(\frac{k_b T m_e}{2\pi\hbar^2} \right)^{3/2} e^{-\frac{c_0}{k_b T}}. \quad (38)$$

Solving the quadratic equation gives

$$X_e = \frac{-c + \sqrt{c^2 + 4c}}{2}, \quad (39)$$

where we have neglected the minus sign, since $\sqrt{c^2 + 4c} > c$, and it does not make sense to have $X_e < 0$. For large c , we can Taylor expand the square root in Eq. 39 to get

$$\begin{aligned} X_e &= \frac{1}{2}(-c + \sqrt{c^2 + 4c}) \\ &= \frac{1}{2} \left(-c + c\sqrt{1 + \frac{4}{c}} \right) \\ &\approx \frac{1}{2} \left(-c + c \left(1 + \frac{2}{c} \right) \right) \\ &= \frac{1}{2}(-c + c + 2) \\ X_e &\approx 1, \end{aligned}$$

when c is very large. In our code we have used this approximation when $\frac{1}{c} < 10^{-4}$.

When $X_e \leq 0.99$ we switched to the Peebles equation, since the Saha equation is only valid close to equilibrium. We solved the Peebles equation using a Runge-Kutta 4 solver, just as we did in Section II.

After computing the free electron fraction X_e , we computed the optical depth τ from Eq. 33, and the visibility function \tilde{g} from Eq. 34. Eq. 33 was solved using the same Runge-Kutta 4 solver as for the Peebles equation, with the initial condition $\tau(x=0) = 0$, and then Eq. 34 was solved directly from $\tau(x)$.

We also computed the times x , z and t for decoupling and recombination, where we use $\tau = 1$ for decoupling, and $X_e = 0.1$ for recombination, and we computed the freeze-out abundance of electrons $X_e(x=0)$.

Lastly we computed the sound-horizon at decoupling r_s by solving Eq. 36 with initial condition $s(x_{\text{ini}}) = \frac{c_s(x_{\text{ini}})}{\mathcal{H}(x_{\text{ini}})}$, again using the Runge-Kutta 4 solver.

C. Results

In Fig. 10 we have plotted the free electron fraction X_e as a function of the scalefactor a , including what it

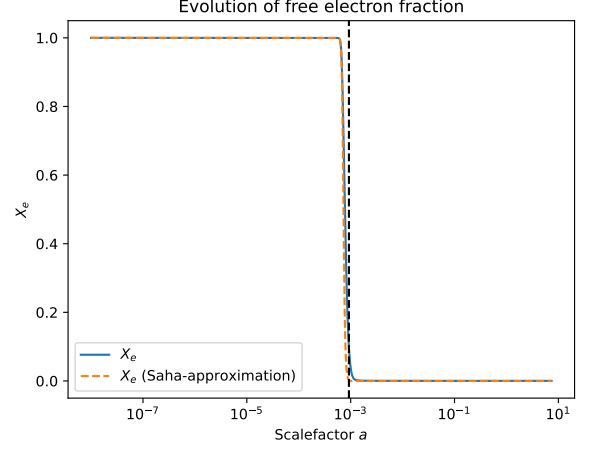


FIG. 10. The free electron fraction X_e as a function of the scalefactor a . The dashed orange curve represents X_e according to the Saha approximation, and the vertical dashed line shows the scalefactor at recombination.

would look like if we used the Saha-approximation the whole time. We see that $X_e = 1$ at very early times. This is exactly what we would expect, since the early universe was too hot for electrons to bind to protons and form hydrogen atoms, thus all electrons in the universe were free. When the temperature drops sufficiently, recombination happens, and the electrons start binding to protons in the universe, creating stable hydrogen atoms. This can be seen in Fig. 10 by X_e beginning to drop rapidly at around $a = 9.3 \cdot 10^{-4}$ (marked by a vertical dashed line). Today the universe mostly consists of bound atom states, which is why we see X_e stabilizing close to zero after recombination, at $X_e = 2.0 \cdot 10^{-4}$. It is more apparent in Fig. 11 that the free electron fraction is not exactly zero. This figure is identical to Fig. 10, except with a logarithmic y -axis. Here we also see that the Saha approximation keeps decreasing rapidly, and it actually reaches zero.

There are several reasons why the free electron fraction today is not actually zero. Although the number of protons and electrons in the universe overall are the same (the universe is electrically neutral), some parts of space will contain more or less protons than electrons. As the universe expands, the particles spread further, and these uneven distributions of electrons and protons increase. In the parts of space where the distribution is uneven, there will be leftover electrons or protons after recombination that are too far apart to form hydrogen atoms. In addition, even though the average temperature of the photons has decreased, there will still be some high-energy photons left. These high-energy photons can still rip atoms apart into protons and electrons.

In Fig. 12 we can see the evolution of the optical depth τ and it's first and second derivatives. We can see that τ starts out very large, meaning we would not be able to see anything in the very early universe due to photons scat-

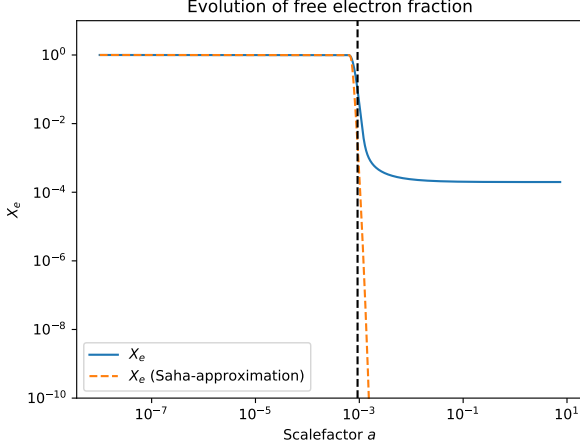


FIG. 11. The same plot as in Fig. 10, but here with a logarithmic y -axis to better show the difference between the predicted free electron fraction, and how it would look according to the Saha approximation.

tering off free electrons. τ then slowly decreases until it reaches recombination, represented by a vertical dashed line, where it drops rapidly. This is because the free electrons in the universe starts forming bound hydrogen atoms at this point, which means photons can start moving more freely. After recombination, the optical depth starts decreasing slowly again, and continues in that way until today. The slow decrease in the optical depth before and after recombination comes from the expansion of the universe. As the universe expands, the free electrons become less dense, giving photons more room to move. The effect of the expansion of the universe is however not as significant as when the number of free electrons decreases during recombination, which is why the slope is much less steep before and after recombination than during.

In Fig. 13 we see the visibility function \tilde{g} as a function of x , as well as its first and second derivatives. In the early universe, $\tilde{g} = 0$, which corresponds well with our description of a dense universe with photons scattering off free electrons before being able to move anywhere. At recombination the free electrons bind to protons, forming hydrogen atoms, giving photons room to move. Therefore, the photons we observe today have a high probability of coming from recombination, which is why \tilde{g} peaks at recombination, represented by a vertical dashed line in Fig. 13. After recombination, \tilde{g} again goes to zero. This is because the probability of photons we observe today to have last scattered at a time much later than recombination is very low, since there are hardly any free electrons to scatter off of. We often refer to recombination as the surface of last scattering, and this comes from the fact that \tilde{g} , which is a probability distribution for when photons we observe last scattered, peaks at recombination.

In Table II we show the computed times for when de-

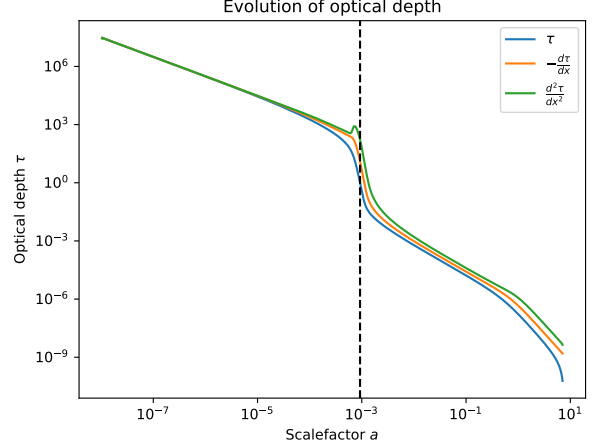


FIG. 12. The optical depth τ , and its first and second derivatives $\frac{d\tau}{dx}$ and $\frac{d^2\tau}{dx^2}$, as functions of the scalefactor a . The vertical dashed line shows the scalefactor at recombination.

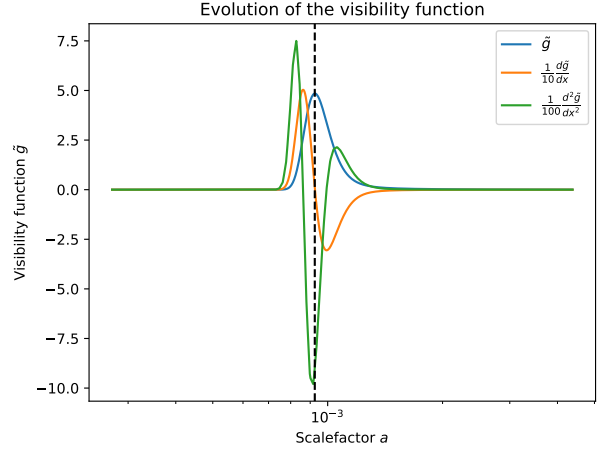


FIG. 13. The visibility function \tilde{g} and its first and second derivatives $\frac{d\tilde{g}}{dx}$ and $\frac{d^2\tilde{g}}{dx^2}$, as functions of the scalefactor a . The derivatives have been scaled to fit in the same figure as \tilde{g} . The vertical dashed line shows the scalefactor at recombination.

coupling and recombination happens. We see that we get a redshift at recombination of $z = 1083$, which compared to the value of $z = 1090$ given in the Planck paper[2] gives a relative error of only 0.6%. After recombination, decoupling happens very quickly, only 1000 years later. This makes sense, as the two are closely related. When the free electrons bind to protons and form hydrogen, the photons decouple as they can start moving more freely.

Lastly, we also computed the sound-horizon $r_s = 164\text{Mpc}$. This value is rather far from the Planck paper[2], which found $r_s = 144\text{Mpc}$, thus giving a relative error of 14%. The fact that our results diverge from the Planck paper[2] could be because we ignore the formation of helium and heavier elements, and reioniza-

TABLE II. Values of scalefactor a , redshift z and cosmic time t at recombination and decoupling.

	a	z	t (Gyr)
Recombination ($X_e = 0.1$)	$9.22 \cdot 10^{-4}$	1083	$4.08 \cdot 10^{-4}$
Decoupling ($\tau = 1$)	$9.24 \cdot 10^{-4}$	1081	$4.09 \cdot 10^{-4}$

tion.

IV. MILESTONE III EVOLUTION OF STRUCTURE IN THE UNIVERSE

The main goal of this paper is to compute the CMB power spectrum, which shows fluctuations in the photon temperature measured from the CMB. So far we have assumed the universe to be homogeneous and isotropic, but this model does not allow for temperature fluctuations. In this milestone we will therefore expand on our current model by considering linear perturbation theory. We will consider perturbations to the FLRW metric, the density and velocity parameters of different constituents of the universe, and the photon temperature, and we will use Einstein's equations and the Boltzmann equation to construct a coupled set of differential equations for these parameters. We will also look at inflation theory as a model to find initial conditions for the different perturbation parameters and find how these evolve throughout the history of the universe. In this way we can begin to see how structures form in the universe as time evolves.

A. Theory

1. Fourier space

Given some function $u(x, t)$ of space and time, the Fourier transform $\hat{u}(k, t)$ is given by

$$\hat{u}(k, t) = \int_{-\infty}^{\infty} dx u(x, t) e^{-ikx}, \quad (40)$$

where k is the wavenumber for a specific Fourier mode $u(x, t) e^{-ikx}$. Likewise, the transformation from Fourier space back to real space is given by

$$u(x, t) = \int_{-\infty}^{\infty} dk \frac{1}{2\pi} \hat{u}(k, t) e^{ikx}. \quad (41)$$

One powerful usage of the Fourier transform is that spatial derivatives disappear when we transform to Fourier space. If we have a spatial derivative of the function $u(x, t)$, the expression transforms as

$$\frac{d^n}{dx^n} u(x, t) \rightarrow (ik)^n \hat{u}(k, t). \quad (42)$$

This is useful for us for two reasons.

a. Simplify differential equations. We want to compute perturbations to a lot of values. The metric potentials, the photon temperature multipoles and the density and velocity perturbations for photons, baryons and dark matter. These values depend on each other, and result in a set of non-linear coupled partial differential equations. Partial differential equations are very hard to solve, but using the Fourier transform, we can reduce these equations to *ordinary* differential equations by removing the spatial derivatives. Ordinary differential equations are much easier to work with, and we can solve these numerically for different values of k .

b. Looking at different scales of the universe. When describing the perturbations in the universe, we don't care too much about how the perturbations look at specific regions in the universe. Our primary interest is to see how the perturbations look at different *scales* of the universe, since the perturbations at different scales give insight to how structures in the universe form, at what scales, and what physical phenomena that drives these formations. When we Fourier transform our equations, we find the time evolution of our perturbation parameters for different Fourier modes, characterized by constant wavenumbers k . The solutions for a specific wavenumber k then gives us the perturbations at a specific scale, given by the wavelength $\lambda \sim \frac{1}{k}$. Thus solving for the perturbations at different Fourier modes gives us the exactly what we want, the evolution of structure formation at different scales of the universe, where larger wavenumber k corresponds to smaller scales, and vice versa.

2. Metric perturbations

Until now, we have assumed the universe to be homogeneous and isotropic, described by the FLRW metric given in Eq. 10. The universe is, however, not truly homogeneous and isotropic. Certain parts of the universe will be more or less dense than other parts of the universe. On very large scales (and here, we are working with the universe as a whole), we expect the universe to be close to homogeneous and isotropic, such that any deviation from the FLRW universe can be considered as linear perturbations. The linearly perturbed FLRW metric that we will consider is given by

$$ds^2 = -dt^2(1 + 2\Psi) + a^2(1 + 2\Phi)(dx^2 + dy^2 + dz^2), \quad (43)$$

where $\Psi(t, \vec{x})$ and $\Phi(t, \vec{x})$ are the linear perturbations to the FLRW metric, and are functions of space and time. In other words, Ψ and Φ describe how the curvature of spacetime deviates from a homogeneous and

isotropic universe at different locations, and at different times. When we say that the perturbations are linear, we mean that Ψ and Φ are sufficiently small that any term with perturbation factors of second order or higher ($\Psi^2, \Phi^2, \Psi\Phi, \Psi^2\Phi, \dots$), can be neglected. The choice of perturbation factors given in Eq. 43 is called the Newtonian gauge, as Ψ corresponds to the gravitational potential in Newtonian mechanics, while Φ is a perturbation to the curvature of space.

3. Other perturbation parameters

We will consider a linear perturbation to the density of each constituent of the universe

$$\rho_i = \bar{\rho}_i(1 + \delta_i), \quad (44)$$

where $\bar{\rho}_i$ is the mean density, δ_i a small perturbation, and i denotes the constituent type (γ for photons, b for baryons and CDM for cold dark matter). We will also consider a linear perturbation to the velocity of each constituent. We don't expect the velocity of particles to have a preferred direction, thus the mean velocity of any constituent is $\vec{0}$, and we denote the velocity perturbation by v_i .

Lastly, we will consider a linear perturbation to the photon temperature

$$T = \bar{T}(1 + \Theta(t, \vec{x}, p, \hat{p})), \quad (45)$$

where \bar{T} is the mean temperature, and Θ the perturbation. The interaction we will consider for photons is Compton scattering, and to first order this interaction does not change the momentum of the photons. Thus we can write $\Theta = \Theta(t, \vec{x}, \hat{p})$. We're going to do computations in Fourier space, thus $\vec{x} \rightarrow \vec{k}$, and for convenience we will combine the direction of \vec{k} and \hat{p} into one variable $\mu = \frac{\vec{p} \cdot \vec{k}}{k}$ (the cosine of the angle between \vec{k} and \vec{p}). We can then write the temperature perturbation as $\Theta(t, k, \mu)$. To simplify calculations, we expand Θ in Legendre multipoles

$$\Theta(t, k, \mu) = \sum \frac{2\ell + 1}{i^\ell} \Theta_\ell(t, k) P_\ell(\mu), \quad (46)$$

where $P_\ell(\mu)$ are the Legendre polynomials, and Θ_ℓ are the photon temperature perturbation multipoles given by

$$\Theta_\ell = \frac{i^\ell}{2} \int_{-1}^1 \Theta(t, k, \mu) P_\ell(\mu) d\mu. \quad (47)$$

4. Perturbation equations

In section II we introduced the Einstein equations given by Eq. 11, and in section III we introduced the

Boltzmann equation given in Eq. 25, with the collision term given in Eq. 26. We will use these equations to find the evolution of the perturbation parameters. Note that when solving for the perturbation parameters we will ignore the different polarizations of the photon multipoles, as well as any contribution from neutrinos.

To solve the Boltzmann equations we will need to consider which interactions are relevant for each particle species. For photons the most relevant interaction is Thomson scattering with electrons

$$e^- + \gamma \rightleftharpoons e^- + \gamma,$$

which is the low-energy limit of Compton scattering. In reality, photons also interact with protons through Thomson scattering, but the Thomson cross section scales as $\frac{1}{m^2}$, where m is the mass of the electron/proton. Since the proton has much higher mass than electrons, the probability of photons scattering with protons is much lower than with electrons, thus we only have to consider Thomson scattering with electrons. Cold dark matter interacts very weakly with other particles, so we will assume no interactions, and set the collision term $C[f]$ in Eq. 25 to zero. Electrons and protons, which we consider collectively as baryons, interact with each other through Coulomb scattering

$$e^- + p^+ \rightleftharpoons e^- + p^+,$$

and with photons through Thomson scattering. As mentioned above, we can neglect the scattering of photons with protons, and consider only Thomson scattering with electrons.

For each of the interaction mentioned above we can find the matrix element $|\mathcal{M}|^2$ given by quantum field theory, and using Eq. 26 we can find the collision term at the right hand side of the Boltzmann equation given by Eq. 25. We can then use the Boltzmann equation to achieve the distribution function f , and from f we can find the energy-momentum tensor given by

$$T_\nu^\mu = \frac{g}{(2\pi)^3} \int \frac{dP_1 dP_2 dP_3}{\sqrt{-\det g}} \frac{P^\mu P_\nu}{P^0} f, \quad (48)$$

where $\det g$ is the determinant of the metric $g_{\mu\nu}$, which in our case is the perturbed FLRW metric given by 43.

We then have the right hand side of Einstein's equation, as given in Eq. 11. Using our perturbed metric, we can compute the Christoffel symbols from Eq. 13, which in turn gives us the Ricci tensor given by Eq. II A 2, and then the Einstein tensor given by Eq. 12. We then find the left hand side of Einstein's equations, and together with T_ν^μ we can find the equations for all the perturbed parameters. The full system of equations we end up with are

Photon temperature multipoles:

$$\Theta'_0 = -\frac{ck}{\mathcal{H}}\Theta_1 - \Phi', \quad (49a)$$

$$\Theta'_1 = \frac{ck}{3\mathcal{H}}\Theta_0 - \frac{2ck}{3\mathcal{H}}\Theta_2 + \frac{ck}{3\mathcal{H}}\Psi + \tau' \left[\Theta_1 + \frac{1}{3}v_b \right], \quad (49b)$$

$$\Theta'_\ell = \frac{\ell ck}{(2\ell+1)\mathcal{H}}\Theta_{\ell-1} - \frac{(\ell+1)ck}{(2\ell+1)\mathcal{H}}\Theta_{\ell+1} + \tau' \left[\Theta_\ell - \frac{1}{10}\Theta_2\delta_{\ell,2} \right], \quad 2 \leq \ell < \ell_{\max} \quad (49c)$$

$$\Theta'_\ell = \frac{ck}{\mathcal{H}}\Theta_{\ell-1} - c\frac{\ell+1}{\mathcal{H}\eta(x)}\Theta_\ell + \tau'\Theta_\ell. \quad \ell = \ell_{\max} \quad (49d)$$

Density and velocity perturbations:

$$\delta'_{\text{CDM}} = \frac{ck}{\mathcal{H}}v_{\text{CDM}} - 3\Phi', \quad (50a)$$

$$v'_{\text{CDM}} = -v_{\text{CDM}} - \frac{ck}{\mathcal{H}}\Psi, \quad (50b)$$

$$\delta'_b = \frac{ck}{\mathcal{H}}v_b - 3\Phi', \quad (50c)$$

$$v'_b = -v_b - \frac{ck}{\mathcal{H}}\Psi + \tau'R(3\Theta_1 + v_b), \quad (50d)$$

$$\delta_\gamma = 4\Theta_0, \quad (50e)$$

$$v_\gamma = -3\Theta_1. \quad (50f)$$

Metric perturbations:

$$\Phi' = \Psi - \frac{c^2k^2}{3\mathcal{H}^2}\Phi + \frac{H_0^2}{2\mathcal{H}^2} \left[\Omega_{\text{CDM}0}a^{-1}\delta_{\text{CDM}} + \Omega_{b0}a^{-1}\delta_b + 4\Omega_{\gamma0}a^{-2}\Theta_0 \right], \quad (51a)$$

$$\Psi = -\Phi - \frac{12H_0^2}{c^2k^2a^2}\Omega_{\gamma0}\Theta_2, \quad (51b)$$

where $R = \frac{4\Omega_{\gamma0}}{3\Omega_{b0}a}$. Together, Eqs. 49-51 define a closed set of non-linear coupled differential equations, and it is this set of equations we will be solving numerically in our code.

5. The tight coupling regime

In the early universe, photons and baryons are tightly coupled to each other. In this regime, the $[\Theta_1 + \frac{1}{3}v_b] = \frac{1}{3}(v_b - v_\gamma)$ in Eq. 49b and the $(3\Theta_1 + v_b) = (v_b - v_\gamma)$ factor in Eq. 50d become very small, while τ' becomes large.

Thus the last term in Eq. 49b and 50d are multiplications of a very small and a very large factor, which quickly gives large errors in the numerical solutions. This makes the system of equations described above numerically unstable in the early universe. We call this regime *tight coupling*, and we will do some changes to the equations in this regime in order to make the system stable. First, we note that since the photons and baryons are tightly coupled in this regime, they move together as one fluid, and thus higher order moments of the photon multipole expansion disappear, leaving only the first two moments Θ_0 and Θ_1 . Using further approximations, we can rewrite the equations for Θ_1 and v_b (which are the ones who caused us trouble) as

$$q = \frac{-[(1-R)\tau' + (1+R)\tau''](3\Theta_1 + v_b) - \frac{ck}{\mathcal{H}}\Psi + (1 - \frac{\mathcal{H}'}{\mathcal{H}})\frac{ck}{\mathcal{H}}(-\Theta_0 + 2\Theta_2) - \frac{ck}{\mathcal{H}}\Theta'_0}{(1+R)\tau' + \frac{\mathcal{H}'}{\mathcal{H}} - 1}, \quad (52a)$$

$$\Theta'_1 = \frac{1}{3}(q - v'_b), \quad (52b)$$

$$v'_b = \frac{1}{1+R} \left[-v_b - \frac{ck}{\mathcal{H}}\Psi + R \left(q + \frac{ck}{\mathcal{H}}(-\Theta_0 + 2\Theta_2) - \frac{ck}{\mathcal{H}}\Psi \right) \right], \quad (52c)$$

where q does not represent anything physical, but is

simply there to simplify the equations for Θ_1 and v_b . For

the rest of the multipole moments, we use the expressions given by the initial conditions (further down), and for the rest of the perturbation parameters we use Eqs. 50-51. The equations for the tight coupling regime are only valid as long as

$$\left| \frac{d\tau}{dx} \right| < 10 \cdot \max \left(1, \frac{ck}{\mathcal{H}} \right), \quad (53)$$

and as long as we have not yet reached recombination.

6. Some problems with our model so far

There are a couple of problems with the model of the universe that we have presented so far.

a. The horizon problem. Firstly, the temperature of the CMB is close to uniform everywhere, meaning that the photon temperature we measure from one direction is nearly the same as the temperature measured from the opposite direction. Photons we receive from opposite directions of the universe should not have been causally connected to each other at the time of recombination, so it is strange that they seem to be in thermal equilibrium.

b. The flatness problem. We observe the universe today to be flat, and have assumed it to be flat at earlier times as well. For the universe to be flat, the universe requires a very specific density of matter and energy. Small deviations to these densities would result in an open or closed universe, yet we observe the universe to be flat today. If we later find that the universe is not flat after all, then we need to understand why it appears so today.

c. The exotic relic problem. Some proposed extensions to the standard model of particle physics theorize that the early universe should produce large quantities of exotic particles, such as magnetic monopoles. However, we have not yet observed such particles, which is weird if they are really produced in such abundance.

d. Initial conditions. This is the problem that is most relevant for us. We want to solve Eqs. 49-51 numerically. In order to do so, we need the initial conditions for each perturbation parameter, thus we need some description the very early universe that can actually give these initial conditions.

7. Inflation

The most widely accepted solution to the problems stated above is the theory of inflation. Inflation describes a very short, very rapid exponential expansion of the universe only moments after the big bang. This theory explains the horizon problem, since photons from different parts of the CMB would be causally connected before inflation. They could therefore be in thermal equilibrium, even though they are so far apart after inflation, due to the rapid expansion. Inflation also solves the flatness problem. If the universe is not flat, but has expanded

very rapidly, the universe we observe today might just be such a small part of the whole universe that we observe it to be flat because it is flat locally. The problem of exotic relics is also solved by inflation. Even though the very early universe might have produced an abundance of exotic particles, the exponential expansion during inflation would spread these particles across the universe, giving a very low density today. In that case, we might have trouble observing them today, even if there were relatively many of them in the early universe.

The last problem we mentioned was the problem of finding initial conditions. Inflation happens only moments after the big bang, thus we can use the time of inflation as the initial conditions for our differential equations. To find the initial conditions, we describe a scalar quantum field ϕ for the inflaton, the theorized particle that drives inflation. We also assume the density perturbations of different particles to be present already at inflation. This assumption leads to what we call the *adiabatic initial conditions*. From these assumptions, we find the initial conditions for Eqs. 49-51 to be

$$\Psi = -\frac{2}{3} \quad (54a)$$

$$\Phi = -\Psi \quad (54b)$$

$$\delta_{\text{CDM}} = \delta_b = -\frac{3}{2}\Psi \quad (54c)$$

$$v_{\text{CDM}} = v_b = -\frac{ck}{2\mathcal{H}}\Psi \quad (54d)$$

$$\Theta_0 = -\frac{1}{2}\Psi \quad (54e)$$

$$\Theta_1 = +\frac{ck}{6\mathcal{H}}\Psi \quad (54f)$$

$$\Theta_2 = -\frac{20ck}{45\mathcal{H}\tau'}\Theta_1, \quad (54g)$$

$$\Theta_\ell = -\frac{\ell}{2\ell+1}\frac{ck}{\mathcal{H}\tau'}\Theta_{\ell-1}, \quad (54h)$$

where again we have ignored polarizations of the photon multipoles and the contributions from neutrinos in the universe.

B. Implementation details

We solve for the perturbation parameters in the tight coupling regime using Eqs. 49a, 50a-50c, 51, 52, and 54g-54h. This is done using a Runge-Kutta 4 solver with initial conditions given by Eq. 54, and we solve up until the time tight coupling ends, given by Eq. 53, but no later than the time of recombination. When we reach the end of tight coupling, we use the resulting values as initial conditions for the full system given by Eqs. 49-51, and solve these equations, again using the Runge-Kutta 4 solver. The solving of the complete set of equations, both before and after the tight coupling regime, is done in Fourier space, so we have to solve all the differential equations for different values of the wavenumber k . We

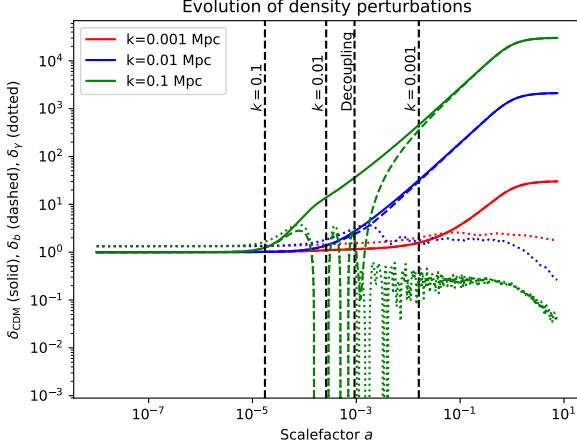


FIG. 14. Evolution of density perturbations for cold dark matter δ_{CDM} , given by solid lines; baryons δ_b , given by dashed lines; and photons δ_γ , given by dotted lines, as functions of the scale factor a . The density perturbations are shown at three different scales, given by $k = 0.001$, $k = 0.01$, and $k = 0.1 \text{ Mpc}$. The vertical dashed line labeled "decoupling" shows the time when decoupling happens. The remaining three vertical lines labeled by the wave number k shows the time when the wave mode of that wave number enters the horizon, i.e., the time when $ck \sim \mathcal{H}$.

have chosen to solve for k -values ranging from $5.0 \cdot 10^{-5}$ to 0.3 Mpc .

C. Results

1. Density perturbations

In Fig. 14 we see the evolution of density perturbations δ_i at different Fourier modes k , for cold dark matter, baryons and photons. The different Fourier modes we consider correspond to different scales of the universe, where a decreasing mode k depicts increasing scale.

Let's first consider the density perturbation δ_{CDM} for dark matter. δ_{CDM} starts at around $10^0 = 1$, which is what we expect from the initial conditions by inserting Eq. 54a into Eq. 54c. It then remains constant at this value for all wave modes until that mode enters the horizon. Before this, the mode represents a scale where different regions are not causally connected, and so the gravitational potentials cannot reach other particles at this scale, and δ_{CDM} cannot grow. After the wave modes enter the horizon, δ_{CDM} starts increasing, meaning dark matter starts to bundle up in certain parts of space, and once it starts increasing, it will keep increasing until today. When dark matter starts accumulating in certain regions of space, they create gravitational wells, which means even more dark matter will move towards those regions. This is why we observe that δ_{CDM} keeps increasing, since a non-uniform density will lead to even

more variations in the density.

When we extrapolate the perturbations to times later than today, we see that δ_{CDM} stops increasing, and stabilizes at a certain value. This is because the universe today mainly consists of dark energy, and the dark energy density keeps increasing. The large abundance of dark energy makes the expansion of the universe accelerate to the point where space expands faster than gravitational wells from dark matter can attract other dark matter particles. When this happens, dark matter will no longer keep accumulating, and the density perturbation δ_{CDM} stabilizes at whatever value it was when this point is reached. The dark matter density perturbation δ_{CDM} behaves in the same way for all Fourier modes, but not at the same time. The larger scales, that is, smaller k , take longer time to enter the horizon, thus the perturbation δ_{CDM} starts increasing later.

The density perturbation δ_b for baryons behaves in a similar way to δ_{CDM} . They both start at the same value, which is expected since their initial condition are both given by Eq. 54c, and they both start to increase at around the same time. For large and intermediate scales, given by $k = 0.001$ and $k = 0.01 \text{ Mpc}$, δ_b follows the curve of δ_{CDM} . For small scales however, δ_b 's curve deviates from that of δ_{CDM} , as can be seen for $k = 0.1 \text{ Mpc}$ in Fig. 14. The reason density perturbations for dark matter and baryons are similar is that they in some ways are very similar particles. They are both non-relativistic, have mass that contribute to spacetime curvature, and they are both strongly affected by that curvature. The main difference between them is that, while dark matter does not interact (or interacts very weakly) with other particles, baryons interact with each other through Coulomb scattering, and with photons through Thomson scattering. Due to the Thomson scattering interaction, baryons and photons are tightly coupled until around recombination, and therefore moves together as one fluid. When baryons group together at certain regions in space, thus causing the density perturbation δ_b to increase, this also causes the photons to cluster, which in turn increases the radiation pressure. Because of this increased pressure, the photon-baryon fluid diffuses, and the density perturbations δ_b and δ_γ both decrease. This decrease in δ_γ causes the pressure to go down, so the baryons can start to cluster again, and so it continues in an oscillatory motion. This keeps going until the photons and baryons decouple. After decoupling the photon density perturbation δ_γ still oscillates due to the battle between gravitational wells and radiation pressure, but the baryons are now free from the photons, and cluster in the same way as dark matter.

For the larger scales with $k = 0.01$ and $k = 0.001 \text{ Mpc}$, the wave mode enters the horizon either after decoupling, or so close to decoupling that the effects from tight coupling are not present. This is why δ_b follows δ_{CDM} at these scales. The photon density perturbation δ_γ increases slightly together with dark matter and baryons due to the gravitational wells they produce, but due

to the high radiation pressure it quickly decreases back down. When δ_γ has decreased, the universe is in an era where the radiation density parameter Ω_R is very low (see Fig. 6), and so the amount of photons is so small that δ_γ does not change much, which is why it stabilizes at this point.

2. Velocity perturbations

In Fig. 15 we see the evolution of the velocity perturbations for dark matter, baryons and photons at the same scales as we considered for density perturbations.

Again, let us first consider the velocity perturbation v_{CDM} of dark matter. At all scales v_{CDM} is steadily increasing until today, and then starts decreasing. Clusters of dark matter move due to gravitational wells, thus deeper gravitational wells causes the dark matter perturbations to move faster. Thus the velocity perturbation v_{CDM} increases since dark matter keeps clustering, causing increasingly deeper gravitational wells. However, v_{CDM} starts decreasing around the time today when the universe becomes dominated by dark energy. Dark energy causes the universe to accelerate, and when the universe accelerates so quickly that it becomes stronger than gravitational effects, the gravitational potentials become shallower, and thus v_{CDM} starts to decrease.

Just like with the density perturbations, the velocity perturbation v_b for baryons act in the same way as v_{CDM} , since they are still very similar particles. And again like the density perturbations, v_b deviates from v_{CDM} at small scales, and starts oscillating before it comes back and behaves like v_{CDM} at the end. This deviation happens around the same time as the deviation of δ_b from δ_{CDM} , when the universe contains a significant amount of photons, and as with δ_b it stems from the fact that photons and baryons are tightly coupled.

The density perturbation δ_γ for photons were oscillating a low, and the same can be seen for their velocity v_γ . This makes sense, since we expect the velocity of the perturbations to move faster when perturbations are stronger. If δ_γ close to zero (meaning that the photon fluid is close to homogeneous) we expect v_γ to be close to zero (because there are no perturbations moving in the fluid). When δ_γ is larger, however, we expect v_γ to be larger, since there are more overdensities in the fluid that can move around.

3. Photon temperature quadrupole

In Fig. 16 we see the evolution of the photon temperature quadrupole moment Θ_2 . In the early universe, Θ_2 is close to zero, and stays at this value until around the time of recombination. When recombination hits, Θ_2 starts oscillating with a frequency that increases as the scale decreases. Θ_2 represents anisotropies in the photon temperature, which is very small in the early universe.

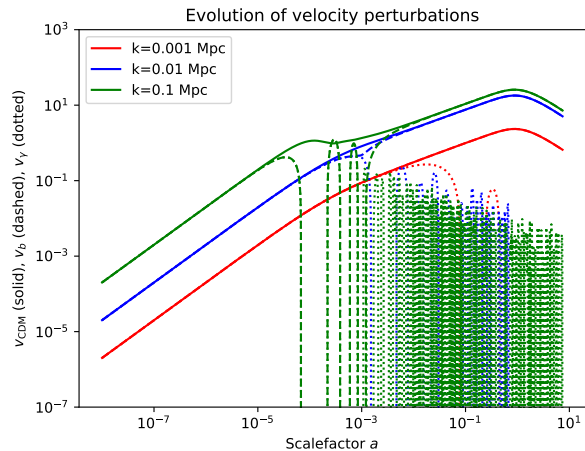


FIG. 15. Evolution of velocity perturbations for cold dark matter v_{CDM} , given by solid lines; baryons v_b , given by dashed lines; and photons v_γ , given by dotted lines, as functions of the scalefactor a . The velocity perturbations are shown at three different scales, given by $k = 0.001$, $k = 0.01$, and $k = 0.1 \text{ Mpc}$.

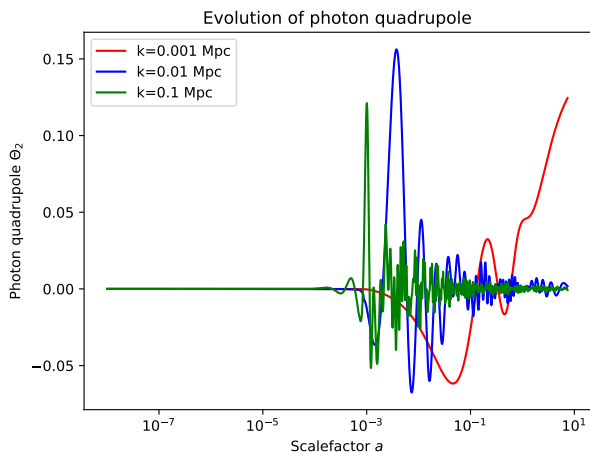


FIG. 16. Evolution of the photon temperature quadrupole moment Θ_2 as a function of the scalefactor a for three different scales, given by $k = 0.001$, $k = 0.01$, and $k = 0.1 \text{ Mpc}$.

After recombination, the photons are free to move further across the universe, and are thus redshifted. This gives a decreasing value of the photon temperature, causing larger fluctuations. The larger scales we look at, however, the fluctuations appear less significant, which is why Θ_2 oscillates less at larger scales.

4. Gravitational potentials

In Fig. 17 we have the evolution of the spatial perturbation Φ to the FLRW metric. At all scales, Φ has a small but non-zero value in the early universe, which is

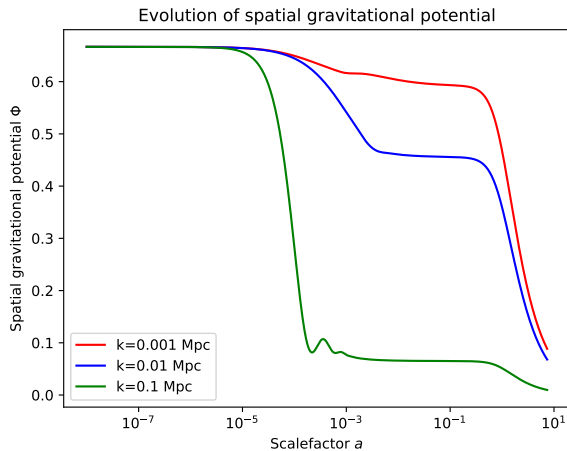


FIG. 17. Evolution of the spatial gravitational perturbation Φ to the FLRW metric as a function of the scalefactor a for three different scales, given by $k = 0.001$, $k = 0.01$, and $k = 0.1\text{Mpc}$.

consistent with the non-uniform density of dark matter and baryons, as shown in Fig. 14, causing gravitational wells in space. Φ stays steadily at its beginning value until it suddenly drops to a lower value where it stabilizes again, and as it approaches today it decreases rapidly again. This is the general trend we see at all scales, but for smaller scales the first drop happens earlier and more drastically, dropping to lower values than at larger scales. The second drop happens around the time when dark energy begins to dominate the universe. As the dark energy density increases in the universe, the expansion rate starts to accelerate. When the universe expands quicker, the distance between gravitational wells at different parts of the universe increases, making the universe appear uniform at smaller and smaller scales, making Φ decrease. In Fig. 18 we see how anisotropic stress $\Phi + \Psi$ evolves with time. In the early universe, $\Phi + \Psi$ is stable at zero, meaning the universe appears isotropic. Around the time of recombination, the anisotropic stress starts to deviate from zero, before stabilizing back at zero after a while.

V. MILESTONE IV THE CMB AND MATTER POWER-SPECTRA

We now have all ingredients needed to get to the heart of the matter, the CMB. In this last milestone, we will use the perturbations from section IV to compute the CMB power spectrum. We start by discussing the line of sight integration method for computing the photon temperature multipoles more efficiently, and decompose these in spherical harmonics in order to consider temperature anisotropies at different angular scales. Finally, we give a more qualitative physical description of what the CMB power spectrum represents, as well as introduce the

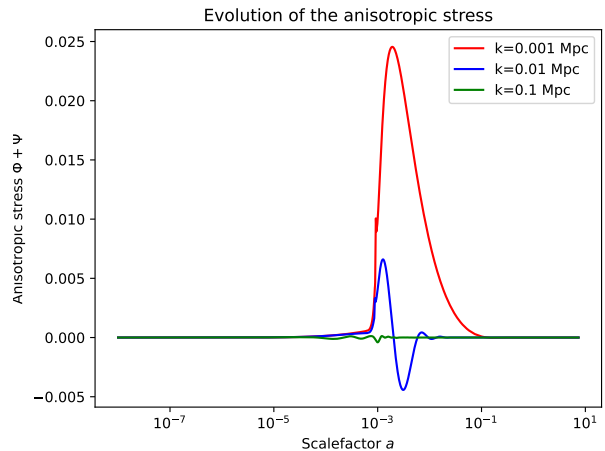


FIG. 18. Evolution of the anisotropic stress $\Phi + \Psi$ as a function of the scalefactor a for three different scales, given by $k = 0.001$, $k = 0.01$, and $k = 0.1\text{Mpc}$.

matter power spectrum. The theoretical predictions we get are compared to data from the Planck paper [2], the SDSS galaxy surveys [10] and results from the WMAP and ACT [4].

A. Theory

1. The line of sight integration

In order to compute the CMB power spectrum, which is the main goal of this project, we need the photon temperature multipoles Θ_ℓ . These can be found by solving the coupled set of differential equations given in Eq. 49, but doing so requires heavy computational work as we want to compute up to $\ell > 1000$. Each Θ_ℓ depends on all previous Θ_ℓ 's, thus this method gives a coupled set of more than 1 000 coupled differential equations. Luckily, physicists Uroš Seljak and Matias Zaldarriaga[12] found a much simpler method for computing Θ_ℓ . This method is called line of sight integration, and substitutes the coupled differential equations with an integration over a source term. Using this method we only have to compute up to Θ_2 using the differential equations in Eq. 49. For $\ell \geq 3$ we can use the line of sight integration given by

$$\Theta_\ell(k, x=0) = \int_{-\infty}^0 \tilde{S}(k, x) j_\ell[k(\eta_0 - \eta)] dx, \quad (55)$$

where $j_\ell(x)$ are the spherical Bessel functions, given by

$$j_\ell(x) = \frac{i^\ell}{2} \int_{-1}^1 P_\ell(x) e^{-ix\mu} d\mu, \quad (56)$$

where $P_\ell(x)$ are the Legendre polynomials; and $\tilde{S}(k, x)$ is the source function in Fourier space, given by

$$\tilde{S}(k, x) = \tilde{g} \left[\Theta_0 + \Psi + \frac{1}{4}\Pi \right] + e^{-\tau} [\Psi' - \Phi'] - \frac{1}{ck} \frac{d}{dx} (\mathcal{H} \tilde{g} v_b) + \frac{3}{4c^2 k^2} \frac{d}{dx} \left[\mathcal{H} \frac{d}{dx} (\mathcal{H} \tilde{g} \Pi) \right], \quad (57)$$

where $\Pi = \Theta_2 + \Theta_0^P + \Theta_2^P$ and Θ_ℓ^P are the polarization multipoles. We do not consider polarization in this project, so we set $\Theta_\ell^P = 0$. The source function consists of four terms, where the first three terms have quite simple physical interpretations.

a. The Sachs-Wolfe effect. The first term in Eq. 57 is the Sachs-Wolfe term,

$$\tilde{g} \left[\Theta_0 + \Psi + \frac{1}{4}\Pi \right],$$

and it is the dominating term to the temperature multipoles given in Eq. 55. At the time of recombination, the universe is not perfectly homogeneous, but consists of gravitational wells and hills due to matter density fluctuations. Photons travelling from dense regions at recombination are redshifted because they need to "climb out" of gravitational wells, thus losing energy, and photons travelling from less dense regions will be blueshifted due to energy gained from "falling down" gravitational wells. This is what's known as the ordinary Sachs-Wolfe effect, and it gives a direct contribution to the observed photon temperature multipoles Θ_ℓ from gravitational potentials Ψ . We can see the Sachs-Wolfe effect more clearly by rewriting the first term of the source function. In Fig. 13 we saw how the visibility function \tilde{g} has a peak at recombination, and is zero at all other times, thus we can approximate $\tilde{g} \approx \delta(x - x_{\text{rec}})$. If we insert this into the line of sight integral given by Eq. 55, and ignore the other terms of the source function we find

$$\Theta_\ell(k, x=0) \approx \left[\Theta_0 + \Psi + \frac{1}{4}\Theta_2 \right]_{\text{rec}} j_\ell[k(\eta_0 - \eta_{\text{rec}})],$$

where we have $\Pi = \Theta_2$ since we ignore polarization. Further noting that the photon quadrupole Θ_2 is close to zero at recombination (see Fig. 16), and the conformal time η is much smaller at recombination than today $\eta_{\text{rec}} \ll \eta_0$, we get

$$\Theta_\ell(k, x=0) \approx (\Theta_0 + \Psi)_{\text{rec}} j_\ell(k\eta_0),$$

where $(\Theta_0 + \Psi)_{\text{rec}}$ represents an effective photon temperature including the red-/blueshift from Ψ , and the Bessel function $j_\ell(k\eta_0)$ comes from mapping the photon anisotropies we observe today to a sphere. Thus the dominating contribution to temperature anisotropies observed today is the Sachs-Wolfe effect, which represents inhomogeneities in the photon temperature at the time of recombination due to gravitational potentials.

b. The integrated Sachs-Wolfe effect. The second term in Eq. 57,

$$e^{-\tau} [\Psi' - \Phi'] = \frac{d(\Psi - \Phi)}{dx} e^{-\tau},$$

represents the integrated Sachs-Wolfe effect. While the ordinary Sachs-Wolfe effect describes photons originating in gravitational potentials at the time of recombination, the integrated Sachs-Wolfe effect describes changes in temperature due to photons travelling through a varying gravitational potential in its path from recombination to today. When a photon enters a gravitational potential, it gains energy and blueshifts, and when it exits it loses energy and becomes redshifted. If the potential is close to constant while the photon moves through, the energy gain and loss are nearly equal, and this does not contribute notably to the photon temperature anisotropy. If, however, the potential becomes deeper or shallower while the photon moves through, the total difference in energy is non-zero, and this contributes to the temperature anisotropy. This is captured in the second term of Eq. 57 by the derivative $\frac{d(\Psi - \Phi)}{dx}$, which gives a contribution to Θ_ℓ for varying gravitational potentials.

c. The Doppler term. The third term in Eq. 57 is the Doppler term,

$$\frac{1}{ck} \frac{d}{dx} (\mathcal{H} \tilde{g} v_b).$$

If we again approximate $\tilde{g} \approx \delta(x - x_{\text{rec}})$, we see that the non-zero contribution from this term is at recombination, where photons and baryons are still tightly coupled. Thus we have $v_b \approx v_\gamma$, so the Doppler term shows the contribution to the temperature multipoles Θ_ℓ from the movement of photon overdensities, or in other words, the effect due to the Doppler effect.

2. Spherical harmonics

If $f(\hat{n})$ is a function defined on the surface of a sphere, where $\hat{n} = (\theta, \phi)$, we can express it as the series

$$f(\hat{n}) = \sum_{\ell=0}^{\infty} \sum_{m=-\ell}^{\ell} a_{\ell m} Y_{\ell m}(\hat{n}), \quad (58)$$

where $Y_{\ell m}$ are the spherical harmonics, and the coefficients $a_{\ell m}$ are given by

$$a_{\ell m} = \int d\Omega_{\hat{n}} f(\hat{n}) Y_{\ell m}^*(\hat{n}). \quad (59)$$

This is similar to our description of Fourier transforms in section IV A 1, where instead of expanding in modes e^{-ikx} in flat space, we expand in the spherical harmonics

$$Y_{\ell m}(\theta, \phi) = (-1)^m \sqrt{\frac{(2\ell+1)(\ell-m)!}{4\pi(\ell+m)!}} P_{\ell m}(\cos(\theta)) e^{im\phi}, \quad (60)$$

where $P_{\ell m}$ are the associated Legendre polynomials; and instead of the wavenumber k , they are described by ℓ and m . ℓ gives the number of nodal lines on the sphere, which are lines where the spherical harmonics are zero, and m gives the number of modes along equator.

Fourier transforms are useful when describing the structures in the universe, since it gives insight into the physics happening at different scales rather than at specific points in space. In the same way, spherical harmonics are useful when looking at the CMB photons. Since the photons reach us from different directions in the sky, we can evaluate their temperature as a function on the unit sphere, and expand this function in spherical harmonics. The initial conditions given by inflation are stochastic, so the temperature of photons from specific directions are not interesting to us, but expanding in spherical harmonics gives us a way to describe photons coming from different regions of the CMB based on how far apart in the CMB they originated. Much in the same way as the Fourier transform gives us a description of structures at different scales, the spherical harmonics allow us to compare the CMB temperature at different scales of the CMB, based on how far apart the photons reaching us were at recombination.

3. The CMB power spectrum

In order to test the theory presented so far, we need a way to tie it together with physical observables that can be measured experimentally. If we rewrite Eq. 45 (and remember that we can ignore the p -dependence of Θ), we have

$$\frac{T - \bar{T}}{\bar{T}} = \frac{\delta T}{\bar{T}} = \Theta(\vec{x}, \hat{p}, t), \quad (61)$$

where $\delta T = T - \bar{T}$. When we detect photons from the CMB experimentally, \vec{x} is our position, \vec{p} is the direction on the sky where photons hit the detectors, and t is the time today. We can expand Θ in spherical harmonics, which gives

$$\Theta(\vec{x}, \hat{p}, t) = \sum_{\ell=1}^{\infty} \sum_{m=-\ell}^{\ell} a_{\ell m}(\vec{x}, t) Y_{\ell m}(\hat{p}), \quad (62)$$

and using Eq. 59 we find the coefficients to be

$$a_{\ell m}(\vec{x}, t) = \int d\Omega_{\hat{p}} Y_{\ell m}^*(\hat{p}) \Theta(\vec{x}, \hat{p}, t). \quad (63)$$

We can look at the Fourier transformed temperature perturbation $\Theta(\vec{k}, \hat{p}, t)$, and find

$$a_{\ell m}(\vec{x}, t) = \int \frac{d^3 k}{(2\pi)^3} e^{i\vec{k} \cdot \vec{x}} \int d\Omega_{\hat{p}} Y_{\ell m}^*(\hat{p}) \Theta(\vec{k}, \hat{p}, t). \quad (64)$$

The coefficients $a_{\ell m}$ follow a Gaussian distribution, and the power spectrum C_{ℓ} is given by

$$\langle a_{\ell m} a_{\ell' m'}^* \rangle = C_{\ell} \delta_{\ell \ell'} \delta_{m m'}, \quad (65)$$

where the angle brackets $\langle \cdot \rangle$ denote an ensemble average over several realizations. In our case the realizations are different universes, but we only have one universe to do experiments in (obviously). To work around this problem, we use the fact that the power spectrum for some fixed ℓ is the same for all modes m , so we can approximate the power spectrum as

$$\hat{C}_{\ell} = \frac{1}{2\ell + 1} \sum_{m=-\ell}^{\ell} |a_{\ell m}|^2, \quad (66)$$

where there are $2\ell + 1$ values of m , since it ranges from $-\ell$ to ℓ . The assumption that an average over modes approximates an average over universes is known as the *ergodic hypothesis*, which states that an ensemble average is equal to a spatial average over one realization. Note that, since m ranges from $-\ell$ to ℓ , we have more samples to average from when ℓ is larger. Thus for large ℓ Eq. 66 is a good approximation to the power spectrum C_{ℓ} , but for low ℓ the approximation has a large uncertainty known as *cosmic variance*.

To find an expression for C_{ℓ} we expand $\Theta(\vec{k}, \hat{p}, t)$ in multipoles, and compute C_{ℓ} directly from Eq. 65. We measure the photons today, so we are interested in $\Theta_{\ell}(k) \equiv \Theta_{\ell}(k, x = 0)$. We find

$$C_{\ell} = \frac{2}{\pi} \int k^2 P(k) |\Theta_{\ell}(k)|^2 dk, \quad (67)$$

where

$$P(k) = \frac{2\pi^2}{k^3} \mathcal{P}_{\mathcal{R}}(k) \quad (68)$$

is the primordial power spectrum with

$$\mathcal{P}_{\mathcal{R}} = A_s \left(\frac{k}{k_{\text{pivot}}} \right)^{n_s - 1}, \quad (69)$$

where A_s is the primordial amplitude, n_s is the spectral index, and k_{pivot} is the pivot wavenumber. We can also rewrite Eq. 67 as

$$\frac{dC_{\ell}}{d(\log k)} = 4\pi \mathcal{P}_{\mathcal{R}} \Theta_{\ell}^2(k), \quad (70)$$

which is convenient when we want to solve for C_{ℓ} numerically.

4. A qualitative, non-mathematical intuition for the CMB power spectrum.

In the early universe photons and baryons are tightly coupled, moving as one fluid. This fluid compresses due to gravitational wells, which are mainly caused by overdensities in dark matter. These compressions are then counteracted by radiation pressure from the photons. In regions of underdensities in dark matter, we get gravitational hills, causing decompressions in the photon-baryon

fluid, also counteracted by radiation pressure. This battle between gravity and pressure causes acoustic oscillations in the fluid. In the same way sound propagates by compressing and decompressing the air it moves through, the compressions and decompressions of the photon-baryon fluid propagate as sound waves throughout the universe. As for our perturbation equations, we can look at these sound waves at different scales by decomposing them into plane waves of different wavelengths. When recombination happens, the sound waves stop oscillating, and the photons start moving freely. At this point, wave modes that are at maximum compression or decompression give rise to the largest temperature fluctuations in the CMB, as their photons are red-/blueshifted the most (see section V A 1 a on the Sachs-Wolfe effect). We can choose a specific mode such that the photon-baryon fluid has just enough time to compress once from big bang to recombination. This is the mode with a wavelength two times the sound horizon at recombination, i.e., the distance sound waves can travel from big bang to recombination, although it is more interestingly characterized by the wavenumber $k_1 = \frac{2\pi}{\lambda}$, where λ is the wavelength. The mode with wavenumber $2k_1$ has had just enough time to compress then decompress, the mode with wavenumber $3k_1$ has had time to compress, decompress and then compress again, and so on. This modes give rise to peaks in the CMB power spectrum for specific ℓ 's (where $\ell \propto k$). In the following we will present qualitatively how some of the parameters in our model will affect the CMB power spectrum.

a. Curvature. The first peak in Fig. 21 is closely related to the geometry of the universe. When we measure the size of hot or cold regions in the CMB, we observe the angular size and use euclidean trigonometry to infer their real spatial size. If the universe is flat, this will give us the correct sizes, but if the universe is closed the regions will appear larger than they really are, and if the universe is open they will appear smaller. Thus if the universe is curved, the angular scale we measure the peaks at will shift toward the left or the right. In other words, the position of the peaks give important information about the geometry of the universe.

b. Baryon loading. If the amount of baryons in the universe increases, they will fall deeper into the gravitational wells due to the added weight before the radiation pressure from photons manage to push them back. This leads to stronger compressions, and thus larger redshift in the photons at recombination. The decompressions, however, stay the same, so the photons from gravitational hills are not more blueshifted. Thus for an increase in baryons we expect the odd peaks, corresponding to compressions, to increase in height compared to the even peaks, corresponding to decompressions. This effect is known as *baryon loading*.

c. Radiation driving. If the universe is radiation dominated, this radiation contributes most to the energy density of the universe, and thus also to the gravitational potentials. Therefore, radiation will cause gravitational

potentials, and the photon-baryon fluid is compressed. But since radiation is also the main contributor to pressure, it cannot cluster in the same way as matter does, so the gravitational potentials will decay. Thus by the time the fluid has reached maximal compression, the potential is gone, and there is nothing fighting the radiation pressure as it starts the decompression phase. The amplitude of the acoustic oscillations then increase a lot, causing higher peaks in the CMB power spectrum. This is called *radiation driving*, and only affects the CMB power spectrum at modes that started oscillating during radiation domination. The universe was only radiation dominated at very early times, so we expect to see the effect of radiation driving for modes with shorter wavelengths, as these start oscillating earlier. Thus we expect peaks in the CMB power spectrum to increase in height when we reach sufficiently high ℓ 's. The value of ℓ where radiation driving comes into play depends on the radiation to matter ratio. If we increase the radiation density Ω_R , or decrease the matter density Ω_M while keeping Ω_R fixed, radiation driving will affect the acoustic oscillations for a longer time, thus increasing the height of the peaks for lower ℓ 's.

d. Diffusion damping. Recombination does not happen instantly, so when photons and baryons decouple, the photons have time to scatter around, bouncing from baryon to baryon, before they are released. This process of scattering photons can be modeled as a random walk. We can consider modes with very small wavelengths, that is, scales where hot spots (regions of maximum decompression) and cold spots (regions of maximum compression) are very close. Since the hot and cold spots are close, photons from hot spots have time to scatter to cold spots during recombination, and vice versa. The temperature differences then even out, since the hot spots will contain photons from cold spots and vice versa, and the peaks in the CMB power spectrum will go to zero. This is known as *diffusion damping*, and happens when scales are small, that is, when ℓ is very high. We therefore expect the peaks in the CMB power spectrum to "die out" as ℓ increases, and go to zero.

5. The matter power spectrum

We also want the matter power spectrum $P(k, x)$, which is given by

$$P(k, x) = |\Delta_M(k, x)|^2 P(k), \quad (71)$$

where $P(k)$ is the primordial power spectrum given in Eq. 68, and

$$\Delta_M(k, x) \equiv \frac{c^2 k^2 \Phi(k, x)}{\frac{3}{2} \Omega_{M0} a^{-1} H_0^2} \quad (72)$$

is the total matter density parameter. We measure the matter power spectrum today, so we only need to compute $P(k, x = 0)$. The matter power spectrum tells us

how large the matter density is for regions at a certain distance apart, that is, on certain scales. If $P(k, x = 0)$ is high for some scale given by the wave number k , then the observed matter (typically galaxies) separated by that scale a high density, and are very clustered.

B. Implementation details

We solve the line-of-sight integral given in Eq. 55 to get the photon multipoles Θ_ℓ for ℓ -values up to $\ell = 1200$. This is done using a Runge-Kutta 4 solver with initial conditions $\Theta_\ell(x_{\text{ini}}) = 0$ for all ℓ . We solve for x -values up to $x = 0$, but only store $\Theta_\ell(x = 0)$ since we want the power spectrum today. To obtain the CMB power spectrum C_ℓ we solve Eq. 70, also using a Runge-Kutta 4 solver with initial conditions $C_\ell(k_{\text{ini}}) = 0$ for all ℓ . We multiply the result by a factor $\frac{\ell(\ell+1)}{2\pi}(10^6 T_{\text{CMB}0})^2$ to get units of $(\mu K)^2$. Lastly, we compute the matter power spectrum $P(k, x)$ by solving Eq. 71 directly. When solving for the primordial power spectrum $P(k)$ in Eq. 68, which we need for both the CMB and matter power spectrum, we set the primordial amplitude to $A_s = 2.1 \cdot 10^{-9}$, the spectral index to $n_s = 0.965$ and the pivot wavenumber $k_{\text{pivot}} = 0.05/\text{Mpc}$.

C. Results

1. Photon multipoles

In Fig. 19 we have the photon multipoles $\Theta_\ell(k)$ for different ℓ . We see that $\Theta_\ell(k)$ oscillate for all ℓ , which is consistent with the appearance of the spherical Bessel functions, which are oscillating functions, in the line of sight integral in Eq. 55. The next thing to notice is that $\Theta_\ell(k)$ seems to decrease when we increase either ℓ or k . This is even more apparent in Fig. 20, where we can see the scaled square photon multipoles $\frac{\Theta_\ell^2 H_0}{ck}$ for the same ℓ -values as in Fig. 19. Here we see that $\frac{\Theta_\ell^2 H_0}{ck}$ decreases very rapidly for increasing ℓ or k , which is why we have included three different subplots to show the values at different orders of magnitude. This rapid decline shows that we can neglect $\frac{\Theta_\ell^2 H_0}{ck}$ when ℓ becomes very large. In Eq. 67 we see that, if we ignore constants and insert the primordial power spectrum $P(k)$, the integrand goes as $k^{n_s-1} \frac{|\Theta_\ell(k)|^2}{k}$. We have set the spectral index to $n_s = 0.965$, so the integrand really goes as $\frac{|\Theta_\ell(k)|^2}{k^{1.135}}$. Thus, since $\frac{\Theta_\ell^2 H_0}{ck}$ disappears for large ℓ , so does the integrand in Eq. 67, and so does C_ℓ . Thus we can look at a finite number of relatively few C_ℓ 's, and ignore higher values. The ℓ 's tell us what scales of the CMB we are looking at. For small ℓ we are comparing photons coming from opposite directions in the sky, and for higher ℓ 's we are comparing photons that are closer together. Therefore it makes sense physically for C_ℓ to decrease rapidly when

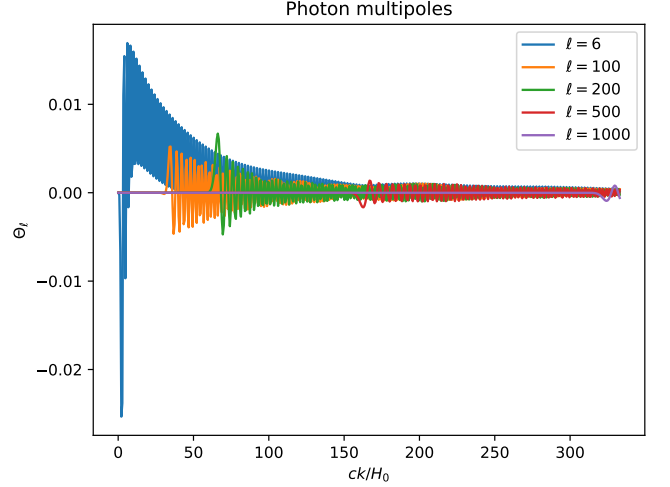


FIG. 19. Photon multipoles Θ_ℓ as functions of the scaled wavenumber ck/H_0 for a couple of selected values of ℓ .

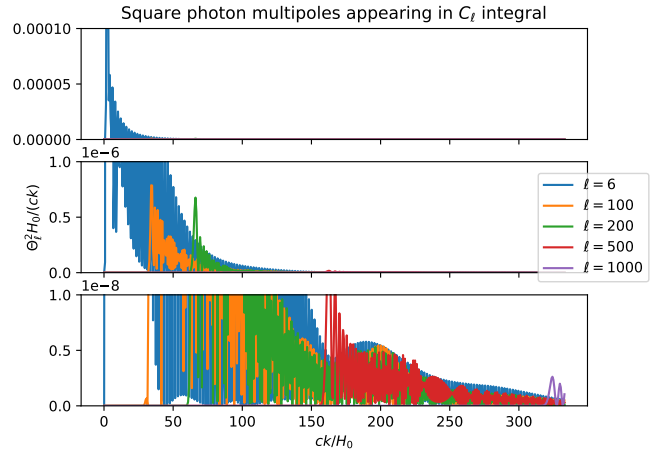


FIG. 20. The squared photon multipole Θ_ℓ divided by the wavenumber k as it appears in the integrand of Eq. 67 as functions of the scaled wavenumber ck/H_0 for a couple of selected values of ℓ . The y -axis is scaled differently for each of the three subplots in order to capture the different details, but their contents are exactly the same.

increasing ℓ , since for high enough ℓ 's we would compare photons at such small scales that we are essentially comparing single photons to themselves, and in that case we would not expect the temperature to vary.

2. The CMB power spectrum

In Fig. 21 we see the CMB power spectrum compared to data from the Planck paper [2].

a. The Sachs-Wolfe plateau. The Sachs-Wolfe plateau refers to the part of the CMB power spectrum at low ℓ 's, where $\ell(\ell+1)C_\ell$ is relatively constant. This part of the spectrum shows the temperature fluctuations at

very large scales, such that they are only affected by the primordial power spectrum. The fact that our prediction for the Sachs-Wolfe plateau in Fig. 21 fits well with the Planck data shows that the way we model the primordial power spectrum, and thus the way we describe the initial conditions set up by inflation, coincides well with reality. Another thing to note with this part of the power spectrum is how large the errorbars are. This stems from the ergodic hypothesis, and shows how the uncertainty of measurements and predictions become very high when we look at low ℓ 's.

b. The first peak. The position of the first peak is closely related to the curvature parameter Ω_K . In Fig. 21 we see that the first peak in our model spectrum happens at around the same ℓ as the peak in the Planck data. Thus the position of the first peak indicates that the universe is close to flat, as our choice of $\Omega_K = 0$ gave a good fit to the Planck data. The height of the first peak is mainly affected by the baryon loading and radiation driving effects. In Fig. 21 the first peak of our model is slightly shorter than that of the Planck data. In our model, we have neglected the contribution from neutrinos when considering the evolution of structure in the universe. Neutrinos have very small masses, and contribute very little to the overall matter density, but instead it contributes strongly to radiation. If we had included neutrinos, we would expect the energy density ratio of radiation to matter to increase, and thus the effect of radiation driving to increase. This should result in the first peak being slightly higher, and so it is reasonable to assume that our lack of neutrinos is the main reason the first peak of the Planck data is somewhat higher than our model predicts.

c. The second and third peak. In Fig. 21, we see that the second peak from our prediction follows the Planck data closely, while the third peak is too high, and a bit shifted to the left. This could be due to our baryon density being too high, which would result in odd peaks being too large. However, decreasing the baryon density would also decrease the height of the first peak, which is not what we want. We notice that the second and third peak of the Planck data have around the same height, while the third peak of our model is higher than the second. A way to make these even out is to increase the radiation of the universe, as this would make the radiation driving effect contribute for larger scales, increasing the second peak. In other words, part of the reason the third peak of our model is higher than the second peak is that we have not included neutrinos in the evolution of structures.

d. The damping tail. For very small scales, that is, high multipoles ℓ , we observe that the spectrum in Fig. 21 goes to zero. This is consistent with the effect of diffusion damping, and the fact that our model coincides well with the Planck data at this point is a good consistency check, indicating that recombination truly happened, and that it happened in the way we have described it.

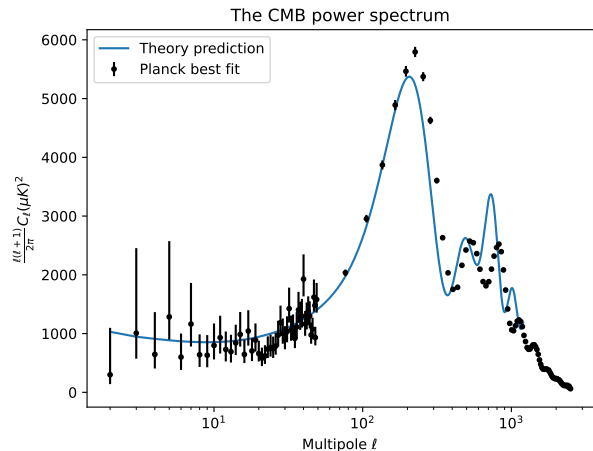


FIG. 21. The CMB power spectrum C_ℓ as a function of the multipoles ℓ . Our predictions are compared to the Planck data [2].

3. The matter power spectrum

In Fig. 22 we have the predicted matter power spectrum from our model, compared with data from SDSS [3] and WMAP/ACT [4]. We see that the power spectrum is very low for small scales (high k), then increases for larger scales until matter-radiation equality, and then decreases again for larger scales. The small scales correspond to a radiation-dominated universe, where the large radiation pressure prevents matter from clustering. This is why the power spectrum is low for small scales, and increases for larger scales, as matter begins to dominate. The large scales correspond to a matter-dominated universe, and at these scales gravitational effects overcome the radiation pressure. However, as the scale increases (meaning we look at effects at later times), the scalefactor increases. Thus for large scales, especially when the amount of dark energy becomes significant, the gravitational effects have to compete with the expansion rate, and the power spectrum decreases. The peak of the power spectrum is at the shift between radiation and matter domination regimes, as indicated by the vertical dashed line in Fig. 22. We see that our prediction for the matter power spectrum takes on too high values compared to the data. This is especially noticeable in the radiation dominated regime (large k). We have not included neutrinos when computing the density perturbations, and since neutrinos contribute significantly more to radiation pressure than to matter density, we expect the power spectrum to be lower if we had included this.

4. The CMB temperature map

Lastly, in Fig. 23 we have included the CMB temperature map. This map shows temperature anisotropies

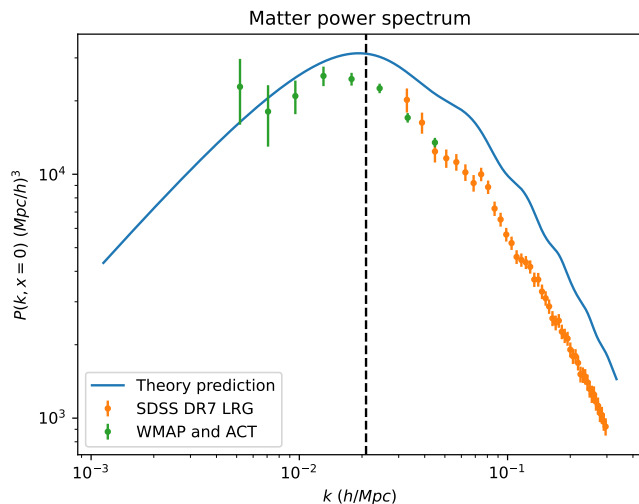


FIG. 22. The matter power spectrum $P(k, x=0)$ as a function of the wavenumber k . Our predictions are compared to data from the galaxy surveys (SDSS DR7 LRG) [3] and the power spectrum inferred from WMAP and ACT [4]. The vertical dashed line shows the wavenumber at matter-radiation equality.

generated by drawing random numbers from a Gaussian distribution with variance $\frac{C_\ell}{\sqrt{2}}$. It is fun to see how the temperature varies, and a visual map like this can increase the intuition of what the CMB really looks like,

but this map does not give any physical insight that we have not already covered in the CMB power spectrum.

VI. CONCLUSION

In this paper we have looked at how the universe has evolved since the big bang, and we did so in four milestones, each building on the previous, and finally leading up to the CMB power spectrum. We found that our prediction for the CMB power spectrum was not a perfect match. The first peak was too low, and the third peak was too high. Both of these could be reasonably explained by our lack of neutrinos when modeling perturbation parameters. If we had included neutrinos, the energy density ratio of radiation to matter in the universe would go up, resulting in increased radiation driving. Consequently, the peaks would align better with the observations. The same goes for the matter power spectrum, which takes on higher values than it should, especially in the radiation dominated regime. Again, the inclusion of neutrinos would increase the radiation causing the matter power spectrum to take on lower values, and thus get closer to the observed data.

If I were to continue the work on this model, it would definitely be interesting to include photon polarization and neutrinos when computing the perturbations, and see if this would lead to a better fit as I expect.

-
- [1] A. A. Penzias and R. W. Wilson, *A Measurement of Excess Antenna Temperature at 4080 Mc/s.*, *Astrophys. J.* **142** (1965) 419–421.
 - [2] N. Aghanim, Y. Akrami, *et. al.*, *Planck2018 results: Vi. cosmological parameters*, *Astronomy & Astrophysics* **641** (2020) A6.
 - [3] B. A. Reid, W. J. Percival, *et. al.*, *Cosmological constraints from the clustering of the sloan digital sky survey dr7 luminous red galaxies*, *Monthly Notices of the Royal Astronomical Society* (2010).
 - [4] R. Hlozek, J. Dunkley, *et. al.*, *The atacama cosmology telescope: A measurement of the primordial power spectrum*, *The Astrophysical Journal* **749** (2012) 90.
 - [5] H. A. Winther, H. K. Eriksen, Ø. Elgarøy, D. F. Mota, and H. Ihle, *Cosmology II a course on the formation of the cosmic microwave background and structures in the universe*, 2021–2024.
 - [6] P. Callin, *How to calculate the cmb spectrum*, 2006.
 - [7] W. Hu, “Cmb tutorials.” Website: <http://background.uchicago.edu/index.html>.
 - [8] M. Betoule, R. Kessler, *et. al.*, *Improved cosmological constraints from a joint analysis of the sdss-ii and snls supernova samples*, *Astronomy & Astrophysics* **568** (2014) A22.
 - [9] N. Metropolis, A. W. Rosenbluth, M. N. Rosenbluth, A. H. Teller, and E. Teller, *Equation of State Calculations by Fast Computing Machines*, *The Journal of Chemical Physics* **21** (1953) 1087–1092. <https://pubs.aip.org/aip/jcp/article-pdf/21/6/1087/18802390/1087.1.online.pdf>.
 - [10] R. Reid, “Chi-squared distribution table with sigma values.” <https://www.reid.ai/2012/09/chi-squared-distribution-table-with.html>, 2012.
 - [11] J. R. Gott III, M. Jurić, *et. al.*, *A map of the universe*, *The Astrophysical Journal* **624** (2005) 463–484.
 - [12] U. Seljak and M. Zaldarriaga, *A line-of-sight integration approach to cosmic microwave background anisotropies*, *The Astrophysical Journal* **469** (1996) 437.

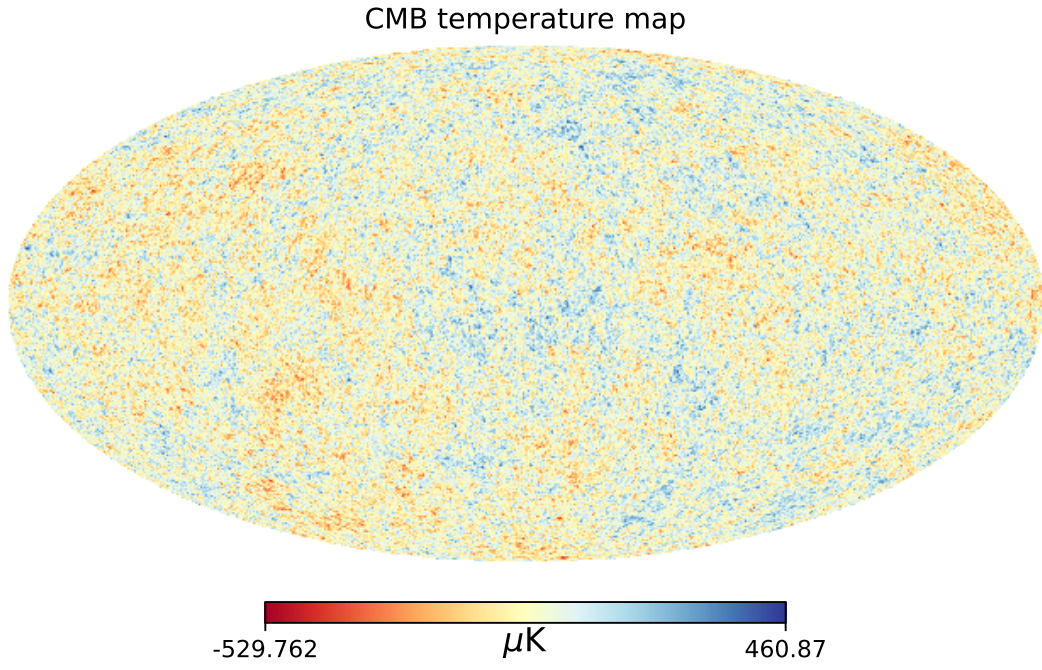


FIG. 23. The CMB temperature map with values drawn from a Gaussian distribution with variance $\frac{C_\ell}{\sqrt{2}}$.